A&A 634, A78 (2020)
https://doi.org/10.1051/0004-6361/201936697

Astronomy & Astrophysics

New chemical scheme for giant planet thermochemistry

Update of the methanol chemistry and new reduced chemical scheme

O. Venot[1], T. Cavalié[2,3], R. Bounaceur[4], P. Tremblin[5], L. Brouillard[6], and R. Lhoussaine Ben Brahim[1]

[1] Laboratoire Interuniversitaire des Systèmes Atmosphériques (LISA), UMR CNRS 7583, Université Paris-Est-Créteil, Université de Paris, Institut Pierre Simon Laplace, Créteil, France
e-mail: olivia.venot@lisa.u-pec.fr
[2] Laboratoire d'Astrophysique de Bordeaux, Univ. Bordeaux, CNRS, B18N, allée Geoffroy Saint-Hilaire, Pessac 33615, France
[3] LESIA, Observatoire de Paris, Université PSL, CNRS, Sorbonne Université, Université Paris Diderot, Sorbonne Paris Cité, 5 place Jules Janssen, 92195 Meudon, France
[4] Laboratoire Réactions et Génie des Procédés, LRGP UMP 7274 CNRS, Université de Lorraine, 1 rue Grandville, BP 20401, 54001 Nancy, France
[5] Maison de la Simulation, CEA, CNRS, Univ. Paris-Sud, UVSQ, Université Paris-Saclay, 91191 Gif-sur-Yvette, France
[6] Université de Bordeaux, 351 Cours de la Libération, 33400 Talence, France

Received 13 September 2019 / Accepted 13 December 2019

ABSTRACT

Context. Several chemical networks have been developed to study warm (exo)planetary atmospheres. The kinetics of the reactions related to the methanol chemistry included in these schemes have been questioned.
Aims. The goal of this paper is to update the methanol chemistry for such chemical networks based on recent publications in the combustion literature. We also aim to study the consequences of this update on the atmospheric compositions of (exo)planetary atmospheres and brown dwarfs.
Methods. We performed an extensive review of combustion experimental studies and revisited the sub-mechanism describing methanol combustion in a scheme published in 2012. The updated scheme involves 108 species linked by a total of 1906 reactions. We then applied our 1D kinetic model with this new scheme to the case studies HD 209458b, HD 189733b, GJ 436b, GJ 1214b, ULAS J1335+11, Uranus, and Neptune; we compared these results with those obtained with the former scheme.
Results. The update of the scheme has a negligible impact on the atmospheres of hot Jupiters. However, the atmospheric composition of warm Neptunes and brown dwarfs is modified sufficiently to impact observational spectra in the wavelength range in which *James Webb* Space Telescope will operate. Concerning Uranus and Neptune, the update of the chemical scheme modifies the abundance of CO and thus impacts the deep oxygen abundance required to reproduce the observational data. For future 3D kinetics models, we also derived a reduced scheme containing 44 species and 582 reactions.
Conclusions. Chemical schemes should be regularly updated to maintain a high level of reliability on the results of kinetic models and be able to improve our knowledge of planetary formation.

Key words. astrochemistry – planets and satellites: atmospheres – planets and satellites: composition – methods: numerical – planets and satellites: gaseous planets – brown dwarfs

1. Introduction

Knowledge of the deep composition of the Solar System giant planets is essential to constrain their formation models (Pollack et al. 1996; Boss 1997; Owen et al. 1999; Gautier & Hersant 2005). While only in situ measurements can provide ground truth measurements, their deep composition remains generally inaccessible to remote sensing techniques or the interpretation of the data has to rely on assumptions regarding temperature (e.g., de Pater & Richmond 1989; de Pater et al. 1991; Luszcz-Cook & de Pater 2013; Cavalié et al. 2014; Li et al. 2018). Even if plans for future in situ exploration exist (Arridge et al. 2012, 2014; Mousis et al. 2014, 2016, 2018), the Galileo probe in Jupiter is the only such experiment that has been carried out (Atreya et al. 1999; Wong et al. 2004). Therefore, thermochemical modeling remains a tool that is complementary to remote observations to infer the deep composition of the Solar System giant planets (Lodders & Fegley 1994; Visscher & Fegley 2005; Visscher et al. 2010; Cavalié et al. 2017).

For H-dominated exoplanets, thermo- and photochemistry are used to predict the atmospheric composition (Moses et al. 2011; Venot et al. 2012). The atmosphere of hot exoplanets is schematically divided into three parts: (1) the deepest, which is very hot, has a chemical composition governed by thermochemical equilibrium; (2) the middle has a lower temperature and a composition controlled by transport-induced quenching; and (3) the upper layers are subject to photochemistry (Madhusudhan et al. 2016, their Fig. 1). Brown dwarfs are also subject to a transition between thermochemical equilibrium (part 1) and a quenching zone (part 2), but photochemistry can be ignored in this case because the object is isolated (e.g., Griffith 2000). To interpret observations of brown dwarf and exoplanet atmospheres probing the regions governed by quenching (and eventually also influenced by photochemistry for exoplanets), we must evaluate correctly the quenching level and abundances of species at this level. It is of particular interest to explain which species are the reservoir of carbon (CO/CH_4) and nitrogen (NH_3/N_2). Indeed, the relative abundances of these species may

vary depending on the pressure and temperature of the quenching level: at high temperatures and/or low pressures CO and N_2 are the main carbon- and nitrogen-bearing species, respectively, while at low temperatures and/or high pressures CH_4 and NH_3 dominate.

One of the main parameters in thermochemical modeling is the chemical scheme. Venot et al. (2012) propose a chemical scheme built with input data from the combustion industry for H, C, O, and N species, which is relevant for temperature and pressure ranges found in the deep tropospheres of the Solar System giant planets, i.e., in hot Jupiters, warm Neptunes, and brown dwarfs. However, Moses (2014) find differences between the latter model and hers in the chemistry of oxygen species that results in significant discrepancies in the abundances of some key (and observable) species, such as CO in the Solar System giant planets. This has been confirmed by Wang et al. (2016). Moses (2014) identify the chemistry of methanol (CH_3OH) as being at the root of the differences. This has motivated the present study, in which we re-evaluate the chemistry of CH_3OH of Venot et al. (2012) and produce a new chemical scheme that accounts for these updates. We also produce a new reduced chemical scheme based on this new scheme, following Venot et al. (2019), for future 3D kinetic modeling.

In this paper, we present a short review of methanol combustion studies (Sect. 2), our new CH_3OH sub-scheme, and its validation (Sect. 3). We then apply it to typical cases (Sect. 4), analyze the differences with the previous model results (Sect. 5), and discuss their implication for atmospheres (Sect. 6). We give our conclusion (Sect. 7). We present in Appendix D a reduced chemical scheme extracted from the update for future 3D models.

2. Short review of methanol combustion experimental studies

The aim of Venot et al. (2012) was to propose a full and robust mechanism to model the combustion of compounds such as hydrogen, methane, and ethane. Their chemical scheme, hereafter V12, which consisted in 105 species involved in 957 reversible and 6 irreversible reactions has been questioned by Moses (2014), pointing more specifically the reaction between methanol and hydrogen radical yielding to methyl radical and water ($CH_3OH+H \rightleftharpoons CH_3+H_2O$). This reaction was initially proposed by Hidaka et al. (1989), with kinetic data for this reaction evaluated by analogy and optimised on a set of experimental data. More generally, the sub-mechanism for methanol combustion in V12 was extracted from the work of Barbe et al. (1995).

Many teams have studied the pyrolysis and combustion of methanol at different concentrations, pressures, temperatures, and with several kinds of reactors. Several studies were performed to measure ignition delay times, for example by Cooke et al. (1971), Bowman (1975), Tsuboi & Hashimoto (1981), and Natarajan & Bhaskaran (1981). These autoignition studies used the shock tube apparatus and employed the reflected shock technique to study autoiignition characteristics at high temperatures (greater than 1300 K) and moderate pressures (5 bar). Kumar & Sung (2011) and more recently Burke et al. (2016) studied the autoignition of methanol in a rapid compression machine for temperatures ranging from 800 to 1700 K and pressures between 1 to 50 bar. These authors show that under these experimental conditions, the ignition delay times of methanol are comparable to the other alcohols.

Several studies have attempted to measure laminar burning velocities for mixtures of methanol and many techniques have been used such as counterflow double flames, burner stabilised flames, the heat flux method, and closed bomb technique. Owing to the high number of studies found in the literature, only the very large study of Liao et al. (2006) is summarised here. These authors studied the influence of the initial temperature and equivalence ratio on the speed flame for an air/methanol mixture at atmospheric pressure. They used a closed bomb apparatus and compared their experimental results to data obtained by other authors with the same experimental setup. The influence of the initial temperature on the laminar flame speed was also studied by Liao et al. (2006). Various equivalence ratios were considered, and an influence of the initial temperature on the laminar flame speed was observed whatever the equivalence ratio. Thus, the laminar burning velocity is almost doubled when the initial temperature increases from 350 to 550 K.

Finally, many other authors have studied the oxidation or pyrolysis of methanol using different reactors (such as static reactor or plug flow reactor) covering a large range of concentration, temperature, and pressure, and these authors have reported species profiles for products and intermediates. Table A.1 gives an overview of the main studies published over the 50 past years on this topic and from which Burke et al. (2016) have built their CH_3OH subnetwork.

3. Validation of a new chemical scheme

Burke et al. (2016) have recently published new experimental data on methanol combustion and propose a revisited chemical model for this species. This kinetic model has been validated against those data and a set of previously published experimental data. The sub-mechanism of methanol is included in a more complete kinetic model to represent the combustion of mixtures with methane, ethane, propane, and butane. Their full model is composed of 1011 reactions and 160 species.

We first extracted the sub-mechanism of methanol combustion and the relevant thermodynamic data from the model of Burke et al. (2016) and updated the original model of Venot et al. (2012) with this new subnetwork (see Table B.1). The main difference from the previous methanol sub-scheme is that some reaction rates have an explicit logarithmic dependence in pressure (see Appendix B). These reactions are presented in Table B.2. Another difference that can be highlighted is that the controversial reaction of Hidaka et al. (1989), $CH_3OH + H \rightleftharpoons CH_3 + H_2O$, is no longer explicitly present in the scheme. The removal of CH_3OH still exists and can eventually lead to the formation of CH_3 and H_2O, but through other destruction pathways (see Sect. 5).

The full and updated chemical scheme that we present in this paper, hereafter called V20, contains 108 species, 948 reversible reactions, and 10 irreversible reactions (i.e., 1906 reactions in total). This scheme can be downloaded from the KInetic Database for Astrochemistry (KIDA; Wakelam et al. 2012)[1].

To validate the inclusion of the Burke et al. (2016) methanol sub-mechanism within our chemical scheme, we compared simulation results with experimental results from various sources (Aronowitz et al. 1979; Cathonnet et al. 1982; Norton & Dryer 1989; Held & Dryer 1994; Ren et al. 2013; Burke et al. 2016). The model performance over a wide array of experimental conditions was found to be in better agreement than that of the original mechanism V12 (see figures in Appendix C).

[1] kida.obs.u-bordeaux1.fr

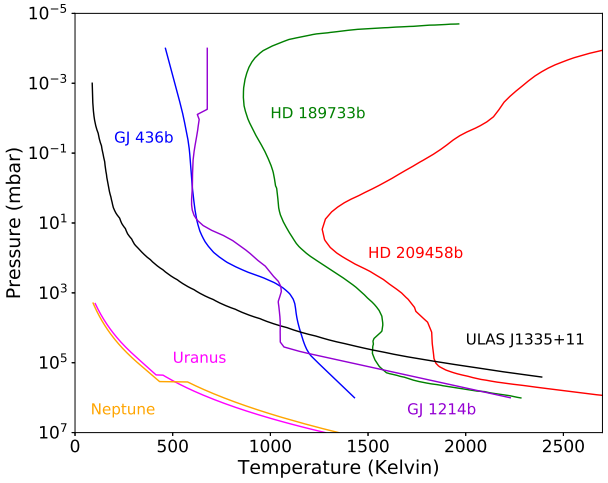

Fig. 1. Adopted thermal profiles of the planets studied in this paper.

With the updated chemical scheme V20, in the next section we revisit the 1D thermo-photochemical model results for emblematic cases published in previous papers: HD 209458b and HD 189733b for hot Jupiters, GJ 436b and GJ 1214b for warm Neptunes, and Uranus and Neptune. We also model for the first time the T Dwarf ULAS J1335+11. Thermal profiles of these planets are shown in Fig. 1.

4. Applications

4.1. Hot Jupiters

We first applied our 1D kinetic model to the atmospheres of HD 209458b and HD 189733b. We used the same thermal (Fig. 1) and eddy diffusion coefficient profiles as Moses et al. (2011); these profiles were used in Venot et al. (2012) with the original chemical scheme. The stellar and planetary characteristics are the same as in Venot et al. (2012). We used solar elemental abundances (Lodders 2010), but we removed 20% of the oxygen to account for sequestration of oxygen in refractory elements of the deep atmospheric layers. As can be seen in Fig. 2, the update of the chemical scheme has a very moderate effect on the chemical composition of these two planets. Whereas quenching levels of all species remain the same in HD 209458b, we notice variations in HD 189733b. With V20, CO_2 is quenched about 100 mbar, whereas it was not with V12; the quenching of CH_4 happens slightly deeper than with V12, indicating that the chemical lifetime of these species is longer with V20. Although still different, this deeper quenching level of CH_4 goes in the direction of the results found by Moses (2014) for this species. However, important differences are still present for the other species presented in this latter paper (i.e., C_2H_2, NH_3, and HCN).

4.2. Warm Neptunes

We studied the effect of the methanol chemistry update on warm Neptunes, which are more temperate planets than hot Jupiters. We applied our 1D kinetic model alternatively using the two chemical schemes to GJ 436b (see Fig. 3), assuming two different metallicities, solar and 100 × solar (100⊙), as well as to GJ 1214b (see Fig. 4), assuming a metallicity 100⊙. For both planets, the thermal profiles used are the same as in Venot et al. (2019), i.e., determined with `ATMO` (Tremblin et al. 2015) for GJ 436b, and the `Generic LMDZ GCM` (Charnay et al. 2015) for

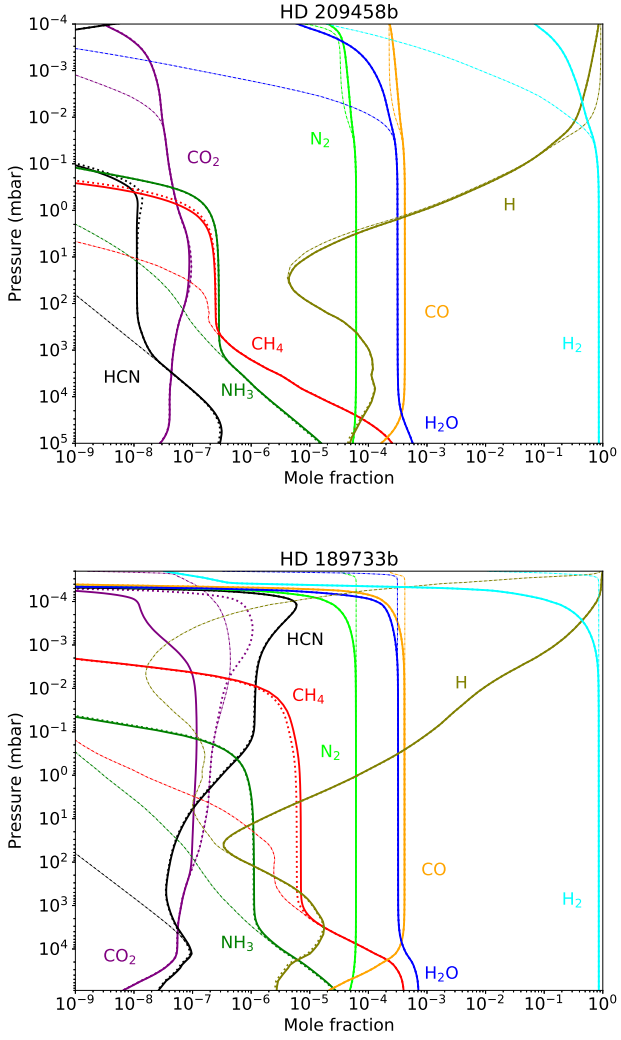

Fig. 2. Vertical abundances profiles of the main atmospheric constituents in two Hot Jupiters: HD 209458b (*top*) and HD 189733b (*bottom*). The abundances obtained with the updated chemical scheme (solid lines) are compared to those obtained with the former scheme of Venot et al. (2012) (dotted lines). Thermochemical equilibrium is shown with thin dash-dotted lines.

GJ 1214b (Fig. 1). For GJ 436b, we assumed a constant eddy diffusion coefficient with altitude, and used two values (10^8 and 10^9 cm^2 s^{-1}). For GJ 1214b, we used the formula determined by Charnay et al. (2015), $K_{zz} = 3 \times 10^7 \times P^{-0.4}$cm^2 s^{-1}, with P in bar. For all the above cases, we observe the same trends: the update of the chemical scheme leads to deeper quenching level, and thus lower abundances for CO, CO_2, and HCN. On the contrary, but for the same reason, CH_4 and H_2O are found to be more abundant (Figs. 3 and 4).

For the model of GJ 436b with a high metallicity, CO and CH_4 have abundances that are very close in the quenching area. With a K_{zz} of 10^8s cm^2 s^{-1}, CO is the main C-bearing species whatever the chemical scheme used, but with a stronger vertical mixing as that presented in Fig. 3 (i.e., $K_{zz} = 10^9$s cm^2 s^{-1}), the main C-bearing species depends on the chemical scheme, i.e., CO with V12 and CH_4 with V20.

4.3. T Dwarfs: ULAS J1335+11

We modeled a typical T Dwarf ULAS J1335+11 (Leggett et al. 2009) with a thermal profile calculated with `ATMO` assuming an

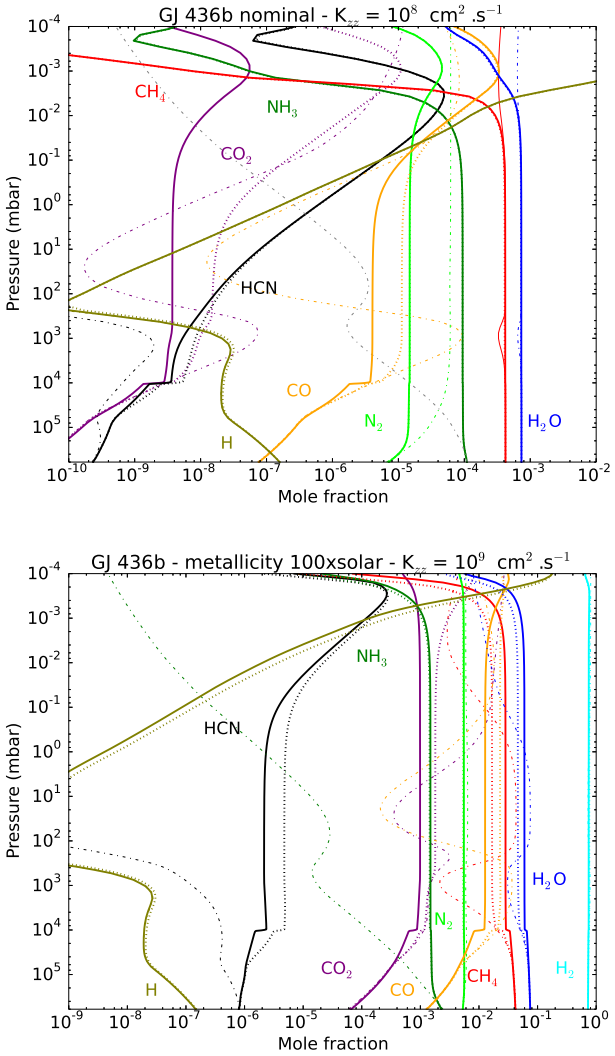

Fig. 3. Same as Fig. 2 for GJ 436b with a solar metallicity and $K_{zz} = 10^8$cm^2 s^{-1} (*top*) and with a 100⊙ metallicity and $K_{zz} = 10^9$cm^2 s^{-1} (*bottom*). With the updated chemical scheme, CO sees its abundance decrease.

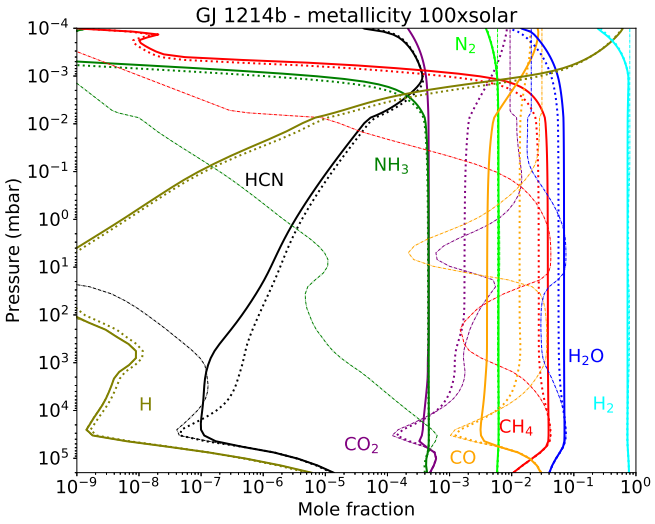

Fig. 4. Same as Fig. 2 for GJ 1214b with a 100⊙ metallicity. As for GJ 436b, with the updated chemical scheme, CO sees its abundance decrease.

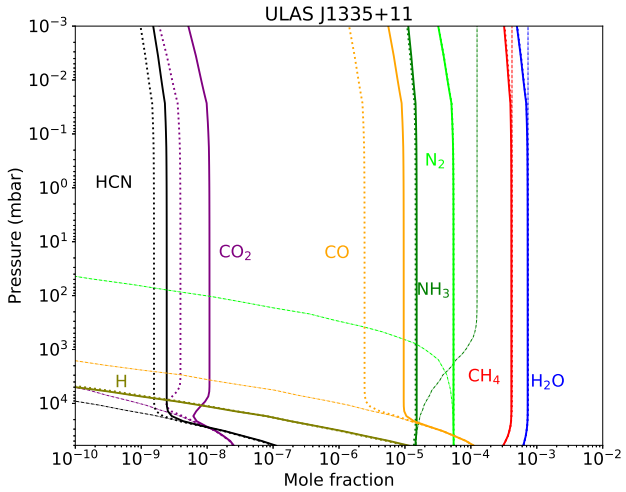

Fig. 5. Same as Fig. 2 for the brown dwarf ULAS J1335+11.

effective temperature of 500 K and a surface gravity of log (g) = 4 (Fig. 1). For the vertical mixing, we assume a constant eddy diffusion coefficient of 10^6 cm^2 s^{-1}. Contrary to warm Neptunes, we observe that with V20 we obtain more CO and CO_2 in the atmosphere than with the former scheme (see Fig. 5) because of the deeper quenching level. The increase in CO abundance is typically of a factor 3 at the effective temperature of late T dwarfs and can impact the CO absorption feature at 4.5 μm (see Sect. 6). At higher effective temperatures closer to the L/T transition, we do not observe any important differences between the updated and former scheme, similar to the hot Jupiter cases.

4.4. Uranus and Neptune

For Uranus and Neptune, the update of the chemical scheme, coupled to the effect of composition on the thermal profile, has a significant effect on the oxygen chemistry. We take the nominal cases of Cavalié et al. (2017) for both planets, i.e., O/H < 160⊙ (Uranus) and = 480⊙ (Neptune), a deep $K_{zz} = 10^8$ cm^2 s^{-1}, an upper tropospheric CH_4 mole fraction of 4%, and a "three-layer" thermal profile. Thus, the model results in upper tropospheric mole fractions of CO of 7.8×10^{-8} and 3.8×10^{-6}, i.e., 34 and 19 times, respectively, above model results using the former chemical scheme and above the observed abundances.

This implies that less H_2O is required in the layers in which thermochemical equilibrium prevails to fit the observations of CO. As a consequence the three-layer temperature profiles are colder than in the nominal cases of Cavalié et al. (2017) because the mean molecular weight gradient at the H_2O condensation level is smaller and therefore produces a less sharp temperature increase in this altitude region. The quench level then occurs deeper, enabling more CO to be transported toward the observable levels. We find that the upper tropospheric CO can be reproduced in Uranus and Neptune with an O/H of <45⊙ and 250⊙. The corresponding model results are shown in Fig. 6. The changes induced by the new chemical scheme are slightly more significant for Uranus than for Neptune.

4.5. Summary

The effect of the update depends on the temperature of the quenching level and on the shape of the abundance profiles. On one hand, if quenching happens at a temperature higher than ∼1500 K and at low pressure (0.1–1 bar, typically what

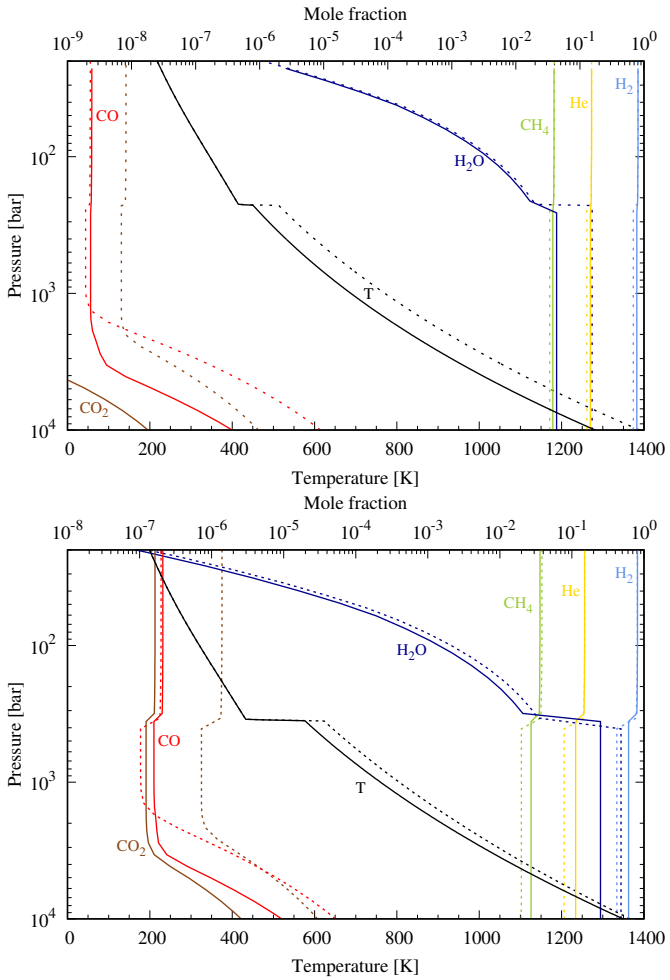

Fig. 6. Vertical abundances profiles of the main atmospheric constituents and oxygen species in Uranus (*top*) and Neptune (*bottom*). The abundances obtained with the updated chemical scheme (solid lines), and O/H <45 and $250\odot$ for Uranus and Neptune (respectively), are compared to those obtained with the former scheme of Venot et al. (2012) (dotted lines), with <160 and $480\odot$ for Uranus and Neptune (respectively). The thermal and abundance profiles are thus not obtained with the same boundary conditions (see text for more details).

happens in hot Jupiters atmospheres tested in this work), no substantial changes occur. On another hand, if quenching happens at lower temperature but higher pressure (>10 bars), then the quenching level is modified, consequently affecting the molecular abundances in upper layers. In all the cases we tested, we observe a deeper quenching level with the updated scheme V20. Molecular abundances are affected by the update depending on their slope at the now deeper quench level. If the abundance increases with altitude, the abundance is lowered (e.g., CO and CO_2 in GJ 436b), and if the abundance decreases with altitude, the abundance is enhanced (CO in Uranus, Neptune, and ULAS J1335+11).

5. Interpretation of the results

5.1. Zero-dimensional model

To understand the changes of kinetics and thus of abundances observed in the atmospheres modeled in this paper, we run our 0D model at the pressure and temperature, where CO is quenched in GJ 436b (i.e., 10 bars and 1150 K) and CH_4 is quenched in HD 209458b (i.e., 0.4 bar and 1500 K) and in HD 189733b (i.e., 1.5 bar and 1500 K), with our chemical schemes.

At the level of CO quenching in GJ 436b (Fig. 7), we observe that the kinetics of CO and CH_4 are much slower with V20 than with V12. The difference is of two orders of magnitude. We identify that this slowdown in the updated scheme is due to the "non-presence" of the reaction $CH_3OH + H \rightleftharpoons CH_3 + H_2O$, which is included in the scheme of V12 with the reaction rate proposed by Hidaka et al. (1989). Adding this unique reaction to our new chemical scheme (hereafter V20+Hidaka) accelerates the kinetics of CH_4 and CO (see Fig. 7, top) and brings the abundances of CO (as well as CO_2 and HCN) in the 1D model very close to that found with V12 (Fig. 8). The difference of CO abundance at 100 mbar is reduced from 7 ppm to 1 ppm (i.e., a factor 2.8 and 1.1 respectively). We note that the change in CO_2 abundance is due to the Hidaka reaction for pressures greater than 1 bar, but also to the reaction $CO + OH \rightleftharpoons CO_2 + H$ for lower pressures.

On the other side, at the levels of CH_4 quenching in HD 209458b and in HD 189733b (Fig. 7, middle and bottom), there is only a minor difference (less than a factor 2) concerning the kinetics of CO and CH_4 in V12 and V20. This explains why we obtain (almost) the same chemical composition for these planets with both chemical schemes. Also, adding Hidaka's reaction to V20 slightly accelerates the kinetics of CO and CH_4, but the variation remains small at about a factor $\sim$2. We can also note that the kinetics of V20+Hidaka is in reality further away from V12 than V20. This excessive acceleration explains the 1D abundance profiles of methane determined for these planets (Fig. 8). CH_4 quenches at (slightly) higher altitude when Hidaka's reaction is included than with the original V20, even higher than what is obtained with V12. For HD 209458b, the deviation of CH_4 abundance at 100 mbar between V12 and V20 is of 4.5 ppb, whereas the gap between V12 and V20+Hidaka is about 20 ppb. These differences are really small, i.e., a factor 1.02 and 1.09, respectively. In the case of CH_4 in HD 189733b (at 10 mbar), the difference between V12 and V20 is a little more important (1 ppm, i.e., a factor 1.2) than the gap between V12 and V20+Hidaka (0.6 ppm, i.e., a factor 1.1). However, compared to the factor 2.8 of deviation observed for CO in GJ 436b, all the differences of CH_4 abundances in hot Jupiters remain really minor. In this case of HD 189733b, it is interesting to compare the methane abundances obtained with those found in Moses (2014). This paper focuses on HD 189733b and compares the atmospheric abundances of several species, including CH_4, obtained using V12 and the Moses et al. (2011) chemical scheme. At 10 mbar, CH_4 has an abundance of $\sim 10^{-5}$ with the Moses et al. (2011) scheme, and $\sim 6 \times 10^{-6}$ with V12 (like in this study). The update of the scheme we perform in this work leads indeed to an increase of CH_4 abundance (to 7×10^{-6}); thus this update is toward the result obtained with the Moses et al. (2011) scheme, but the new value we derive remains lower and is still closer to the previous value obtained with V12.

Finally, we can say that the reaction $CH_3OH + H \rightleftharpoons CH_3 + H_2O$ with the reaction rate of Hidaka et al. (1989), does have a role in the chemical composition of hot Jupiters, but the amplitude of variation generated by the addition of this single reaction in the new V20 scheme remains very small and is not crucial for the kinetics of conversion of CO/CH_4.

5.2. Chemical pathways

To understand the differences between the different panels of Figs. 7 and 8, and thus why the update of the chemical scheme

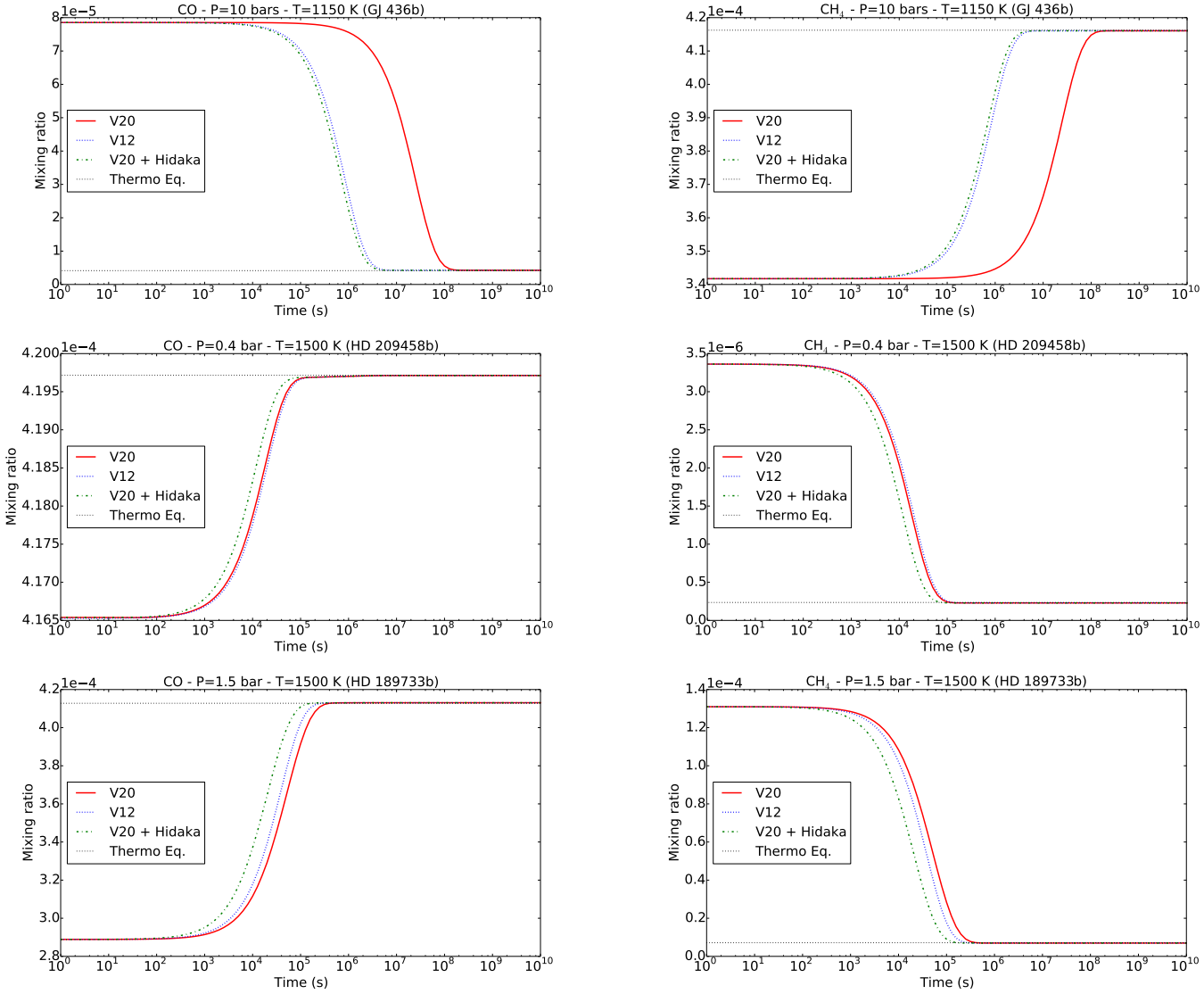

Fig. 7. Temporal evolution of the abundance of CO (*left*) and CH_4 (*right*) at their quenching levels in GJ 436b (*top*), HD 209458b (*middle*), and HD 189733b (*bottom*). The corresponding pressures and temperatures are indicated on each panel. The abundances obtained with the updated chemical scheme (solid red lines) are compared to those obtained with the former scheme of Venot et al. (2012) (dotted blue lines), to the updated chemical scheme to which has been added Hidaka's reaction (dot-dashed green lines) and to the thermochemical equilibrium at these conditions of P and T (dotted black lines). The initial conditions are the thermochemical abundances (assuming solar elemental abundances) at 1 bar and 1100 K (for GJ 436b), at 3.5 bars and 1750 K (for HD 209458b), and at 13 bars and 1570 K (for HD 189733b).

significantly modifies the atmospheric composition of warm Neptunes, T dwarfs, giant planets, but not hot Jupiters, we analyzed the chemical pathways occurring in the different P–T conditions. We found that the behavior of the hydrogen radical is the key to explaining the differences.

At 10 bars and 1150 K (i.e., CO quenching level in GJ 436b), whatever the chemical scheme, the net production rate of H is positive. The kinetic analysis of V12 scheme is represented in Fig. 9. The hydrogen radical comes mainly from metathesis (H-transfer reactions) between H_2 and another radical (R(.)); 75% of H reacts with CO to form HCO, which then reacts mainly with H to give formaldehyde (H_2CO). Then, by addition of H again, H_2CO forms either the CH_2OH or CH_3O radical. These two species, by metathesis, are transformed into methanol; 10% of the hydrogen present in the atmosphere reacts with the formed methanol, through Hidaka's reaction $CH_3OH + H \longrightarrow CH_3 + H_2O$, to form the methyl radical. CH_3 then reacts with H or H_2 to create CH_4. In this P–T condition, with this chemical scheme, 30% of CH_3 comes from Hidaka's reaction. This reaction is thus very important in this context.

We performed the same analysis with the updated scheme (Fig. 10). The production of methanol from H_2 is identical to that of V12. Then, because Hidaka's reaction is not included in this scheme, H cannot react with CH_3OH to form CH_3. In V20 scheme, only 5% of CH_3 comes from methanol, through the priming reaction CH_3OH (+M) $\longrightarrow$ CH_3 + OH (+M). The majority of methyl radical comes from the initiation reactions of methane (CH_4 (+M) $\longrightarrow$ CH_3 + H) and ethane (C_2H_6 (+M) $\longrightarrow$ CH_3 (+M)). Also, CH_3 then reacts with H or H_2 to create CH_4. We see that the main difference between the two chemical schemes is due to the chemical pathways between CH_3OH and CH_3.

We performed the same analysis at 0.4 bar and 1500 K, i.e., CH_4 quenching level in HD 209458b. We find that the main

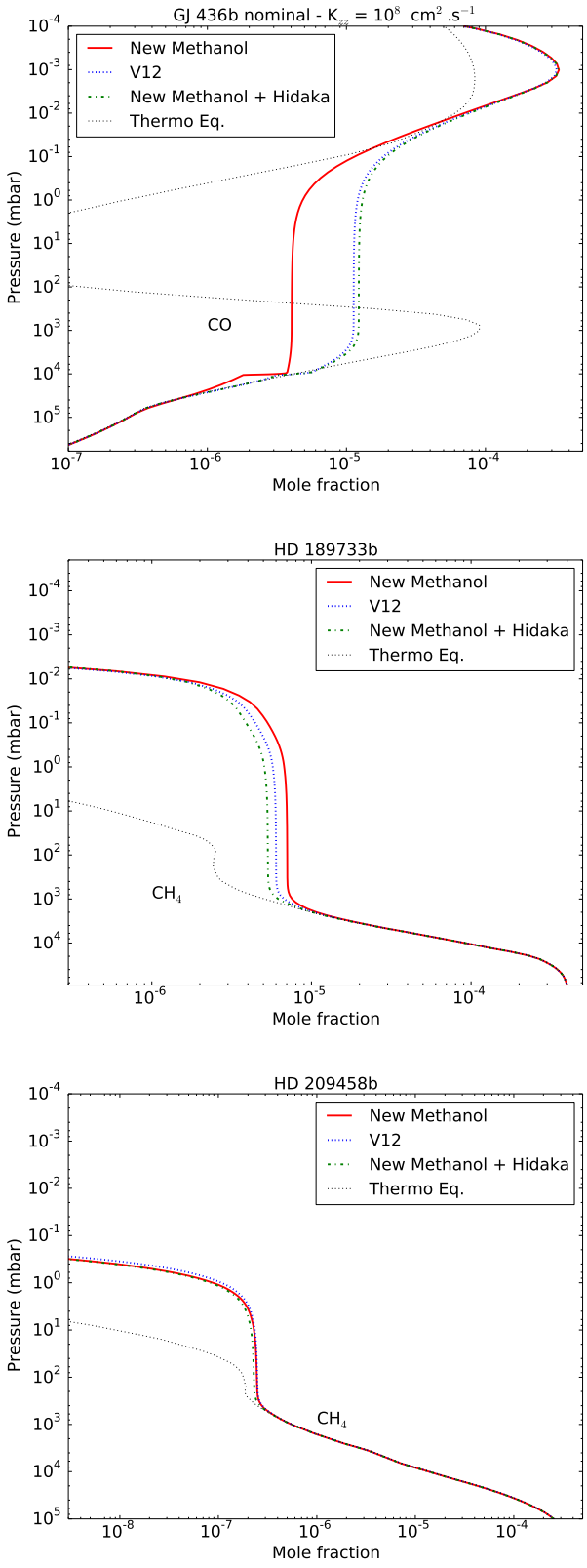

Fig. 8. Vertical abundances profiles of CO in GJ 436b (*top*) and of CH_4 in HD 189733b (*middle*) and in HD 209458b (*bottom*) using different chemical schemes, as labeled.

chemical pathways are the same with the two chemical schemes. Contrary to the previous case, at this lower pressure, the net production rate of H is negative (i.e., positive loss rate). The majority of hydrogen (90%) is equally consumed to give H_2, CH_3, and CH_4. The remaining 10% are involved in the following loop:

$$H + CO \longrightarrow HCO$$
$$HCO + H \longrightarrow CO + H_2.$$

Our analysis shows that at this pressure and temperature, Hidaka's reaction does not step into the overall production/destruction of CH_4, CH_3, and CO, which leads to identical results between the two schemes.

The same analysis has been performed for the quenching level in HD 189733b and leads to the same global conclusion than in HD 209458b. However at this pressure and temperature (1.5 bar and 1500 K), Hidaka's reaction plays a minor role in V12: 0.1% of CH_3 is produced through this reaction (versus 0% and 30% in the cases of HD 209458b and GJ 436b, respectively), which explains why there is a larger difference between V12 and V20 for HD 189733b than for HD 209458b.

To summarise, the key to explaining our results is the production rate of hydrogen. In a P–T domain where the production rate of H is positive, Hidaka's reaction plays a major role in V12 and thus there will be differences between the two schemes. In contrast, in a P–T domain where the loss rate of H is positive, then Hidaka's reaction does not play its rate-accelerating effect and results obtained with the two schemes are very similar.

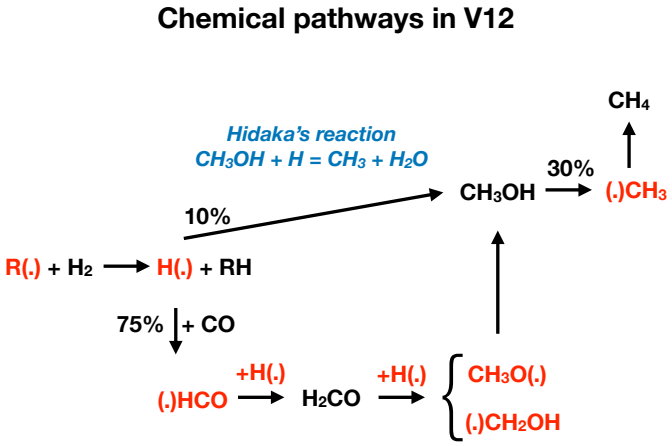

Fig. 9. Chemical pathways controlling $H \leftrightarrow CH_4$ conversion in the chemical scheme of Venot et al. (2012) at 10 bars and 1150 K.

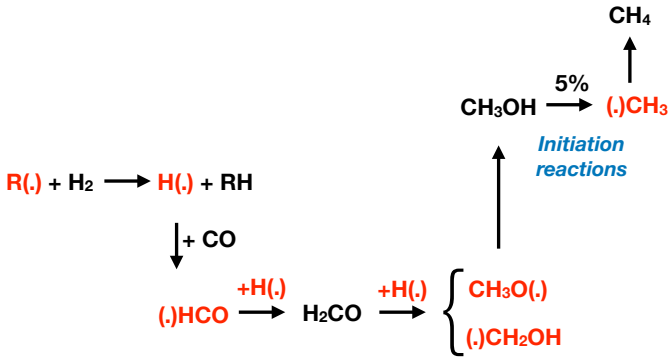

Fig. 10. Chemical pathways controlling $H \leftrightarrow CH_4$ conversion in the updated chemical scheme at 10 bars and 1150 K.

6. Discussion

6.1. Implications for hot Jupiters

The update of the chemical scheme does not fundamentally impact the predicted atmospheric composition of HD 209458b and HD 189733b, which can be considered as typical hot Jupiters with a solar elemental composition. The main variation of abundance is the decrease of CO_2 in the upper atmosphere of HD 189733b. We calculated the synthetic transmission spectra of this planet with the forward model `TauRex` (Waldmann et al. 2015a,b) and observed only a slight variation in the CO_2 absorption band at 4–5 μm (50 ppm). This difference would hardly be distinguishable with future observations performed with *James Webb* Space Telescope (JWST)/Near-Infrared Spectrograph (NIRSpec) or Atmospheric Remote-sensing Infrared Exoplanet Large-survey (ARIEL), with at least one single observation. Stacking together several transits data reduces the error bars, eventually making the distinction possible (Mugnai et al. 2019). Because the abundance of CO_2 is dependent on the quenching level in HD 189733b, an accurate estimation of its abundance could help to constrain and better understand the mixing occurring in the atmospheres of hot Jupiters.

We confirm the abundances of NH_3, HCN, CH_4, and C_2H_2 obtained in Venot et al. (2012) with the previous chemical scheme. Although in the atmosphere of HD 189733b quenching of CH_4 happens deeper than with V12 (leading to a very small increase of the abundance of this species), the other aforementioned species are not affected by the update of the scheme. Thus, our global results are not modified in a way that would bring them closer to the results obtained by Moses (2014). As we explained in Sect. 5, in the atmospheres of hot Jupiters, the differences between our results and those of Moses (2014) are thus not only due to the choice of the reaction rate of $CH_3OH + H \rightleftharpoons CH_3 + H_2O$. This result comforts us with the idea that a global validation of a scheme prevails compared to individual reaction calculations.

6.2. Implications for warm Neptunes

The update of the chemical scheme has important consequences on the molecular composition of warm Neptunes, especially for atmospheres with high metallicities. Because the quenching level of CO_2, CO, and CH_4 is modified, the abundances of these species vary and even a change of the main C-bearing species can occur (Fig. 3). The change of chemical composition found for warm Neptunes has observational consequences.

With the forward model `TauRex`, we computed the synthetic transmission spectra for our models of GJ 436b with a high metallicity. We calculated the spectra corresponding to the compositions at equilibrium, determined with V12 and the updated scheme (Fig. 11). First, we note the important variations between the disequilibrium spectra and those at equilibrium between 1 and 10 μm and in NH_3 band (11 μm), which are the result of the high NH_3 abundance in disequilibrium models. The important departures in CO_2 band (15 μm) result from the high abundance of CO_2 at low pressure in the equilibrium model. We can expect that future high-resolution observations of warm Neptunes such as GJ 436b could be able to detect the possible disequilibrium composition of these planets, even if cloudy (Kawashima et al. 2019), and would certainly help to constrain the vertical mixing responsible of quenched abundances. Then, between the two disequilibrium spectra, important variations are visible in CO_2 absorption bands (4–5 μm, 15 μm). As this species is less abundant with the updated scheme, the absorption is lower in these bands, resulting in a lower $(R_p/R_s)^2$. Such a departure (up to 100 ppm) will be easily observable with future instruments such as JWST/MIRI (Mid-Infrared Instrument). Thus, the choice of the chemical scheme is critical for an accurate constraint on vertical mixing.

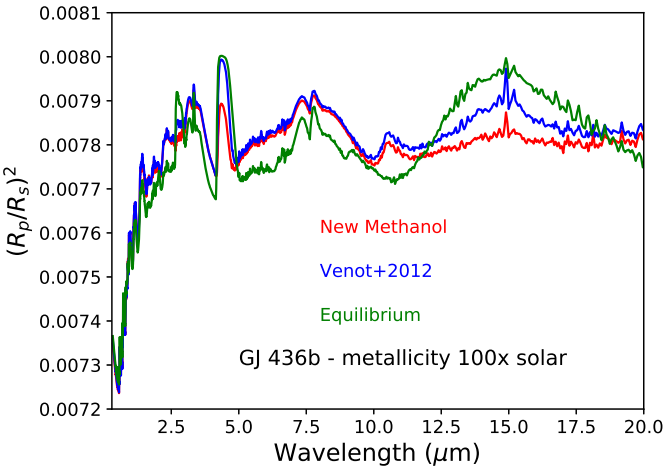

Fig. 11. Synthetic transmission spectra of GJ 436b's atmosphere with a metallicity 100$\odot$. The different spectra correspond to the compositions at chemical equilibrium (green), and with disequilibrium compositions ($K_{zz} = 10^9 \mathrm{cm^2\,s^{-1}}$) calculated with the Venot et al. (2012) scheme (blue), and with the updated scheme (red). The spectral resolving power is 300.

6.3. Implications for brown dwarfs

The updated scheme has a significant impact on the abundance of CO in late T dwarfs. This has a direct impact on the planet spectrum in the 4.7 μm window because CO is a strong absorber at these wavelengths. We show in Fig. 12 the emission spectrum at equilibrium with the former and the updated scheme. The new scheme can lead up to a factor 2 decrease in the flux in this window because of the increase of the CO abundance. Such a difference will be easily constrained by JWST/NIRSpec measurements. The updated scheme combined with JWST measurements will therefore allow us to better characterize the strength of vertical mixing that is necessary to reproduce the out-of-equilibrium abundance of CO in cold brown dwarfs.

6.4. Implications for the formation of Uranus and Neptune

The results obtained for Uranus and Neptune in this paper with the thermochemical model of Venot et al. (2012) and the updated chemical scheme for methanol do not waive the difference found more than two decades ago between the two planets in terms of deep oxygen abundance. This difference primarily results from their different tropospheric CO abundances. While Teanby et al. (2019) recently propose from their *Herschel*-SPIRE data a model without any tropospheric CO in Neptune, i.e., very similar to Uranus, their results probably lack sensitivity in the upper troposphere to make this result robust. Moreno et al. (2011) show in a preliminary combined analysis of *Herschel*-SPIRE and IRAM-30 m data, including the CO(1–0) line that is most sensitive to the tropospheric CO, that the tropospheric CO in Neptune was 0.20 ± 0.05 ppm.

Assuming the CO abundance difference between the two planets is representative of their respective deep oxygen abundances, and according to our new results, only Neptune could

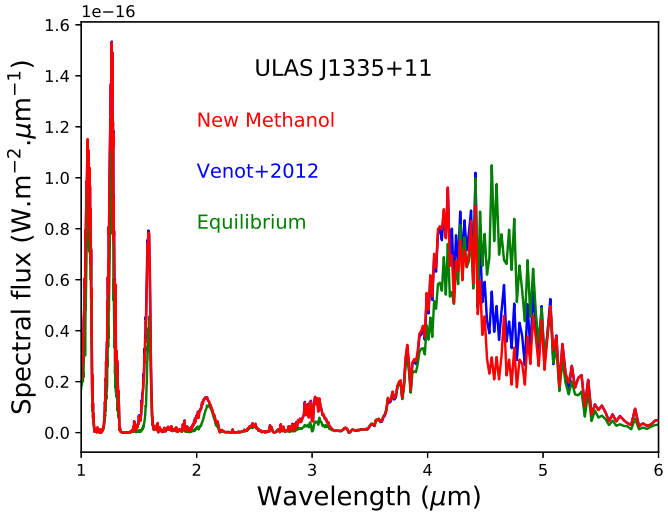

Fig. 12. Emission spectra for ULAS J1335+11 (for $R = 0.1\,R_\odot$ at 10 pc) obtained with the updated chemical scheme (red), compared with those obtained with the former scheme of Venot et al. (2012) (blue) and with equilibrium chemistry (green).

in principle have formed from ices condensed in clathrates (C/O $\sim$ 0.12). On the other hand, the low upper limit on O/H for Uranus is in contradiction with such a process (C/O $\sim$ 1). Interestingly however, this upper limit is close to the C/H required to fit CH_4 (10.383 dex versus 10.331 dex, respectively), which is one of the conditions under which Uranus planetesimal ices could have formed on the CO snow line and be mainly composed of CO rather than H_2O (Ali-Dib et al. 2014). Such a low upper limit may also be derived from inhibited convection in the deep layers of Uranus precluding any tropospheric abundance measurements to be representative of the bulk composition of the planet. We should however not forget that several model parameters remain uncertain such as the deep K_{zz}. A lower K_{zz} than that assumed in our nominal models would result in higher O/H (Cavalié et al. 2017) and therefore change our interpretation.

7. Conclusions

We present in this paper an update of the chemical scheme of Venot et al. (2012). The analysis of Moses (2014) denotes that discrepancies between her results and Venot et al. (2012) could be due to differences in chemical rates involving methanol. This has motivated us to update the Venot et al. (2012) chemical network by replacing their methanol sub-network by that put together by Burke et al. (2016), following a comprehensive study on methanol combustion. We validated this new network against experimental measurements. We emphasize that one change, among others, in our new chemical network is that the controversial reaction $CH_3OH + H \rightleftharpoons CH_3 + H_2O$ has been removed.

The new updated scheme V20 gives very similar results to the former scheme for hot Jupiters. A variation of CO_2 abundance is observed in HD 189733b atmosphere, but only modifies the synthetic spectra to a lower extent (50 ppm at 4–5 μm). A very small change of CH_4 quenching level, which slightly modifies in return the abundance of this species, is also observed in HD 189733b, without any impact on the observable.

For warm Neptunes and T Dwarfs, the update has more significant implications because the reaction $CH_3OH + H \rightleftharpoons CH_3 + H_2$ played an important role in the former scheme of V12. Owing to the quenching of CO, CO_2 (and eventually H_2O and CH_4 in high metallicity atmospheres) happening deeper with the new scheme, the abundances of these species are modified compared to the results obtained with the Venot et al. (2012) chemical scheme. The change is important enough to affect the synthetic spectra. The differences with the former scheme (up to 100 ppm in transmission for warm Neptune and a factor 2 in emission for the T Dwarf) will certainly be detectable with future instruments such as JWST. Using an accurate and updated chemical scheme is thus paramount for a correct interpretation of future observations and for a better comprehension of mixing processes at play in these atmospheres.

The consequence of the update is also fundamental for our understanding of the formation of Uranus and Neptune. For a given O/H ratio, the abundance of CO is higher with the updated scheme than with the former scheme. Consequently, the O/H ratios necessary to reproduce the tropospheric observations of CO are lower than what had been previously found. The updated scheme indicates O/H of <45 and $250\odot$ for Uranus and Neptune, respectively.

Finally, we derived a reduced chemical scheme from this update, for future 3D kinetic models that are crucial (and the next step) for our understanding of (exo)planetary atmospheres. The next steps on the improvement of our chemical scheme will imply adding new species, such as sulphur species, following the recent detection of H_2S in Uranus and Neptune (Irwin et al. 2018, 2019). Phosphorus species could also be of interest to extend the scope of our work, as PH_3 can provide additional constraints on the deep oxygen abundance (Visscher & Fegley 2005). The use of this species as a tracer for O abundance will be possible only if PH_3 is quenched in the atmospheres of giant planets, which is an expected behavior of this molecule Fegley & Lodders (1994); Visscher et al. (2006). However, PH_3 remains undetected in Uranus and Neptune (Moreno et al. 2009). Although these species have not been detected yet in exoplanet atmospheres, their presence is expected and it has been shown that they should be observable with JWST (Baudino et al. 2017; Wang et al. 2017).

We show with this study that collaborations between astrophysicists and combustion specialists are fruitful in order to accurately study high-temperature atmospheres. The intensive work performed in the field of combustion is paramount to perform reliable atmospheric modeling, leading to a correct interpretation of observations.

Acknowledgements. The author thanks the anonymous referee for his/her careful review that helps improving the manuscript. O.V. and T.C. thank the CNRS/INSU Programme National de Planétologie (PNP) and CNES for funding support. P.T. acknowledges support from the European Research Council (grant no. 757858 – ATMO). The authors thank B. Edwards, Q. Changeat, I. Waldmann for useful discussions on JWST and ARIEL observations.

References

Akrich, R., Vovelle, C., & Delbourgo, R. 1978, Combust. Flame, 32, 171
Ali-Dib, M., Mousis, O., Petit, J.-M., & Lunine, J. I. 2014, ApJ, 793, 9
Alzueta, M. U., Bilbao, R., & Finestra, M. 2001, Energy Fuels, 15, 724
Aniolek, K. W., & Wilk, R. D. 1995, Energy Fuels, 9, 395
Aranda, V., Christensen, J. M., Alzueta, M. U., et al. 2013, Int. J. Chem. Kinet., 45, 283
Aronowitz, D., Santoro, R., Dryer, F., & Glassman, I. 1979, Symp. Int. Combust., 17, 633
Arridge, C. S., Agnor, C. B., André, N., et al. 2012, Exp. Astron., 33, 753
Arridge, C. S., Achilleos, N., Agarwal, J., et al. 2014, Planet. Space Sci., 104, 122
Atreya, S. K., Wong, M. H., Owen, T. C., et al. 1999, Planet. Space Sci., 47, 1243
Barbe, P., Battin-Leclerc, F., & Côme, G. M. 1995, J. Chim. Phys., 92, 1666
Baudino, J.-L., Mollière, P., Venot, O., et al. 2017, ApJ, 850, 150
Boss, A. P. 1997, Science, 276, 1836

Bowman, C. T. 1975, Combust. Flame, 25, 343
Burke, U., Metcalfe, W. K., Burke, S. M., et al. 2016, Combust. Flame, 165, 125
Cathonnet, M., Boettner, J. C., & James, H. 1982, J. Chim. Phys., 79, 475
Cavalié, T., Billebaud, F., Dobrijevic, M., et al. 2009, Icarus, 203, 531
Cavalié, T., Moreno, R., Lellouch, E., et al. 2014, A&A, 562, A33
Cavalié, T., Venot, O., Selsis, F., et al. 2017, Icarus, 291, 1
Charnay, B., Meadows, V., & Leconte, J. 2015, ApJ, 813, 15
Chen, J.-Y. 1991, Combust. Sci. Technol., 78, 127
Cooke, D. F., Dodson, M. G., & Williams, A. 1971, Combust. Flame, 16, 233
Cribb, P. H., Dove, J. E., & Yamazaki, S. 1984, in 20th Symp. Int. Combust., 6779
Dayma, G., Ali, K. H., & Dagaut, P. 2007, Proc. Combust. Inst., 31, 411
de Pater, I., & Richmond, M. 1989, Icarus, 80, 1
de Pater, I., Romani, P. N., & Atreya, S. K. 1991, Icarus, 91, 220
Egolfopoulos, F. N., Du, D. X., & Law, C. K. 1992, Combust. Sci. Technol., 83, 33
Fegley, B. J., & Lodders, K. 1994, Icarus, 110, 117
Fieweger, K., Blumenthal, R., & Adomeit, G. 1997, Combust. Flame, 109, 599
Gautier, D., & Hersant, F. 2005, Space Sci. Rev., 116, 25
Gilbert, R. G., Luther, K., & Troe, J. 1983, Ber. Bunsenges. Phys. Chem., 87, 169
Griffith, C. 2000, ASP Conf. Ser., 212, 142
Grotheer, H.-H., Kelm, S., Driver, H. S. T., et al. 1992, Phys. Chem. Chem. Phys., 96, 1360
Held, T., & Dryer, F. 1994, Symp. Int. Combust, 25, 901
Held, T. J., & Dryer, F. L. 1998, Int. J. Chem. Kinet., 30, 805
Hidaka, Y., Oki, T., Kawano, H., & Higashihara, T. 1989, J. Phys. Chem., 93, 7134
Ing, W. C., Sheng, C. Y., & Bozzelli, J. W. 2003, Fuel Process. Technol., 83, 111
Irwin, P. G. J., Toledo, D., Garland, R., et al. 2018, Nat. Astron., 2, 420
Irwin, P. G. J., Toledo, D., Garland, R., et al. 2019, Icarus, 321, 550
Kawashima, Y., Hu, R., & Ikoma, M. 2019, ApJ, 876, L5
Kumar, K., & Sung, C.-J. 2011, Int. J. Chem. Kinet., 43, 175
Leggett, S. K., Cushing, M. C., Saumon, D., et al. 2009, ApJ, 695, 1517
Li, J., Zhao, Z., Kazakov, A., et al. 2007, Int. J. Chem. Kinet., 39, 109
Li, C., Oyafuso, F. A., Brown, S. T., et al. 2018, AGU Fall Meeting Abstracts, 2018, P33F
Liao, S. Y., Jiang, D. M., Huang, Z. H., & Zeng, K. 2006, Fuel, 85, 1346
Lindemann, F. A., Arrhenius, S., Langmuir, I., et al. 1922, Trans. Faraday Soc., 17, 598
Lindstedt, R. P., & Meyer, M. P. 2002, Proc. Combust. Inst., 29, 1395
Lodders, K. 2010, in Principles and Perspectives in Cosmochemistry, eds. A. Goswami, & B. E. Reddy (Berlin, Heidelberg: Springer Berlin Heidelberg), 379
Lodders, K., & Fegley, Jr. B. 1994, Icarus, 112, 368
Luszcz-Cook, S. H., & de Pater, I. 2013, Icarus, 222, 379
Madhusudhan, N., Agúndez, M., Moses, J. I., & Hu, Y. 2016, Space Sci. Rev., 205, 285
Metghalchi, M., & Keck, J. C. 1982, Combust. Flame, 48, 191
Moreno, R., Marten, A., & Lellouch, E. 2009, AAS/Division for Planetary Sciences Meeting Abstracts, 41, 28.02
Moreno, R., Lellouch, E., Courtin, R., et al. 2011, Geophys. Res. Abstracts, 13, 8299
Moses, J. I. 2014, Phil. Trans. R. Soc. London Ser. A, 372, 20130073
Moses, J. I., Visscher, C., Fortney, J. J., et al. 2011, ApJ, 737, 15
Mousis, O., Fletcher, L. N., Lebreton, J.-P., et al. 2014, Planet. Space Sci., 104, 29
Mousis, O., Atkinson, D. H., Spilker, T., et al. 2016, Planet. Space Sci., 130, 80
Mousis, O., Atkinson, D. H., Cavalié, T., et al. 2018, Planet. Space Sci., 155, 12
Mugnai, L., Edwards, B., Papageorgiou, A., Pascale, E., & Sarkar, S. 2019, Eur. Planet. Sci. Congress, 2019, 270
Natarajan, K., & Bhaskaran, K. A. 1981, Combust. Flame, 43, 35
Noorani, K. E., Akih-Kumgeh, B., & Bergthorson, J. M. 2010, Energy & Fuels, 24, 5834
Norton, T., & Dryer, F. 1989, Combust. Sci. Technol., 63, 107
Owen, T., Mahaffy, P., Niemann, H. B., et al. 1999, Nature, 402, 269
Pollack, J. B., Hubickyj, O., Bodenheimer, P., et al. 1996, Icarus, 124, 62
Rasmussen, C. L., Wassard, K. H., Dam-Johansen, K., & Glarborg, P. 2008, Int. J. Chem. Kinet., 40, 423
Ren, W., Dames, E., Hyland, D., Davidson, D., & Hanson, R. 2013, Combust. Flame, 160, 2669
Stewart, P., Larson, C., & Golden, D. 1989, Combust. Flame, 75, 25
Teanby, N. A., Irwin, P. G. J., & Moses, J. I. 2019, Icarus, 319, 86
Tremblin, P., Amundsen, D. S., Mourier, P., et al. 2015, ApJ, 804, L17
Tsuboi, T., & Hashimoto, K. 1981, Combust. Flame, 42, 61
Veloo, P. S., Wang, Y. L., Egolfopoulos, F. N., & Westbrook, C. K. 2010, Combust. Flame, 157, 1989
Venot, O., Hébrard, E., Agúndez, M., et al. 2012, A&A, 546, A43
Venot, O., Bounaceur, R., Dobrijevic, M., et al. 2019, A&A, 624, A58
Visscher, C., & Fegley, Jr. B. 2005, ApJ, 623, 1221
Visscher, C., Lodders, K., & Fegley, B. J. 2006, ApJ, 648, 1181
Visscher, C., Moses, J. I., & Saslow, S. A. 2010, Icarus, 209, 602
Wakelam, V., Herbst, E., Loison, J. C., et al. 2012, ApJS, 199, 21
Waldmann, I. P., Tinetti, G., Rocchetto, M., et al. 2015a, ApJ, 802, 107
Waldmann, I. P., Rocchetto, M., Tinetti, G., et al. 2015b, ApJ, 813, 13
Wang, D., Lunine, J. I., & Mousis, O. 2016, Icarus, 276, 21
Wang, D., Miguel, Y., & Lunine, J. 2017, ApJ, 850, 199
Westbrook, C. K., & Dryer, F. L. 1979, Combust. Sci. Technol., 20, 125
Wong, M. H., Mahaffy, P. R., Atreya, S. K., Niemann, H. B., & Owen, T. C. 2004, Icarus, 171, 153
Yano, T., & Ito, K. 1983, Bull. JSME, 26, 94

Appendix A: Short review of methanol combustion experimental studies

Table A.1. Overview of the main studies published over the 50 past year on the pyrolysis of methanol.

Reference	Reactor	Temperature range (K)	Pressure	Equivalence ratio
Cooke et al. (1971)	A	1570–1879	1 atm	1.00
Bowman (1975)	A	1545–2180	0.18–0.46 MPa	0.375–6.0
Akrich et al. (1978)	F	298	0.11 atm	0.77–1.53
Aronowitz et al. (1979)	B	1070–1225	0.1 MPa	0.03–3.16
Westbrook & Dryer (1979)	A-B	1000–2180	0.1–0.5 MPa	0.05–3.0
Tsuboi & Hashimoto (1981)	A	1200–1800		0.2–2.0
Natarajan & Bhaskaran (1981)	A	1300–1700	0.25–0.45 MPa	0.5–1.5
Cathonnet et al. (1982)	D	700–900	0.02–0.05 MPa	0.5–4.0
Metghalchi & Keck (1982)	F	300–500	0.1 MPa	0.5–1.4
Yano & Ito (1983)	C	700–1000		
Cribb et al. (1984)	A	2000	0.04 MPa	
Hidaka et al. (1989)	A	1372–1842		
Norton & Dryer (1989)	B	1025–1090	0.1 MPa	0.6–1.6
Chen (1991)	D			
Egolfopoulos et al. (1992)	A-B-E-F	820–2180	0.005–0.47 MPa	0.05
Grotheer et al. (1992)	C-F			
Held & Dryer (1994)	B	810–1043	1–10 atm	0.60–1.60
Aniolek & Wilk (1995)	D	650–700	0.92 atm	0.50–1.50
Fieweger et al. (1997)	A	800–1200	12.83–39.48 atm	1.00
Held & Dryer (1998)	A-B-E-F	633–2050	0.026–2 MPa	0.05–2.6
Alzueta et al. (2001)	B	700–1500	1 atm	0.07–2.70
Lindstedt & Meyer (2002)	A-B-F			
Ing et al. (2003)	B	873–1073	1–5 atm	0.75–1.00
Ing et al. (2003)	B	1073	1–10 atm	
Rasmussen et al. (2008)	B	650–1350	1.00 atm	0.004–0.08
Liao et al. (2006)	D	300-550	0.1 MPa	0.6–1.4
Dayma et al. (2007)	D	700–1090	10 atm	0.30–1.00
Li et al. (2007)	A-B-F	300–2200	0.1–2 MPa	0.05–6.0
Noorani et al. (2010)	A	1068–1776	2–12 atm	0.50–2.00
Veloo et al. (2010)	C	343	1 atm	0.70–1.50
Kumar & Sung (2011)	C	850–1100	6.91–29.61 atm	0.25–1.00
Aranda et al. (2013)	B	600–900	20–100 atm	4.35–0.06
Ren et al. (2013)	A	1200–1650	0.1–0.3 MPa	
Burke et al. (2016)	A-C	820–1650	0.2–5 MPa	0.5–2.0

Notes. Reactor types are as follows: shock tube (A), plug flow reactor (B), rapid compression machine (C), stirred reactor (D), static reactor (E), premixed flame (F).

Table A.1 gives an overview of the main studies published over the 50 past years on the pyrolysis of methanol. The CH_3OH sub-network from Burke et al. (2016) that we implemented in our model results from these studies.

Appendix B: New CH_3OH sub-scheme and reactions with a logarithmic dependence in pressure

Under certain conditions, some reaction rate expressions depend on pressure as well as temperature. Generally speaking, the rate for unimolecular/recombination fall-off reactions increases with increasing pressure, while the rate for chemically activated bimolecular reactions decreases with increasing pressure. Several expressions are available in the literature to express the variation of the kinetic data between high and low pressure limit. The Lindemann approach (Lindemann et al. 1922), the Troe form (Gilbert et al. 1983), or the approach taken at SRI International by Stewart et al. (1989) are the main expressions commonly used for the pressure-dependent reactions. The sub-mechanism of methanol combustion uses another kind of expression for the pressure dependence using logarithmic interpolation with the key word PLOG. Miller & Lutz (2003, priv. comm.) developed a generalised method for describing the pressure dependence of a reaction rate based on direct interpolation of reaction rates specified at individual pressures. In this formulation, the reaction rate is described in terms of the standard modified Arrhenius rate parameters. Different rate parameters are given for discrete pressures within the pressure range of interest. When the actual reaction rate is computed, the rate parameters are determined through logarithmic interpolation of the specified rate constants at the current pressure from the simulation. This approach provides a very straightforward way for users to include rate data from more than one pressure regime.

Table B.1 lists the reactions of the new methanol sub-scheme we include in our kinetic model. We list in Table B.2 the

Table B.1. Reactions of the new chemical sub-network of CH_3OH not involving a logarithmic dependence with pressure, extracted from Burke et al. (2016).

Reaction	Rate
$HCOH + O_2 \longrightarrow CO_2 + H + OH$	$k_0 = 8.306 \times 10^{-12}$
$HCOH + O^3P \longrightarrow CO_2 + H + H$	$k_0 = 8.306 \times 10^{-11}$
$HCOH + O^3P \longrightarrow CO + OH + H$	$k_0 = 4.983 \times 10^{-11}$
$HCOH + O_2 \rightleftharpoons CO_2 + H_2O$	$k_0 = 4.983 \times 10^{-11}$
$HCOH + H \rightleftharpoons H_2CO + H$	$k_0 = 3.322 \times 10^{-10}$
$HCOH + OH \rightleftharpoons HCO + H_2O$	$k_0 = 3.322 \times 10^{-11}$
$HOCHO \rightleftharpoons CO + H_2O$	$k_0 = 2.45 \times 10^{12} e^{-30400/T}$
$HOCHO \rightleftharpoons CO_2 + H_2$	$k_0 = 2.95 \times 10^{9} e^{-24390/T}$
$HOCHO + H \longrightarrow H_2 + CO_2 + H$	$k_0 = 7.043 \times 10^{-18} T^{2.1} e^{-2447/T}$
$HOCHO + H \longrightarrow H_2 + CO + OH$	$k_0 = 1.002 \times 10^{-10} T^{-0.35} e^{-1502/T}$
$HOCHO + O^3P \longrightarrow CO + 2\,OH$	$k_0 = 2.94 \times 10^{-6} T^{-1.9} e^{-1496/T}$
$HOCHO + OH \longrightarrow H_2O + CO_2 + H$	$k_0 = 4.352 \times 10^{-18} T^{2.06} e^{-460.5/T}$
$HOCHO + OH \longrightarrow H_2O + CO + OH$	$k_0 = 3.073 \times 10^{-17} T^{1.51} e^{483.7/T}$
$HOCHO + CH_3 \longrightarrow CH_4 + CO + OH$	$k_0 = 6.478 \times 10^{-31} T^{5.8} e^{-1106/T}$
$HOCHO + OOH \longrightarrow H_2O_2 + CO + OH$	$k_0 = 1.661 \times 10^{-12} e^{-5993/T}$
$H_2CO + H\ (+M) \rightleftharpoons CH_2OH\ (+M)$	$\begin{cases} k_0 = 3.504 \times 10^{-16} T^{-4.82} e^{-3283/T} \\ k_\infty = 8.970 \times 10^{-13} T^{0.454} e^{-1810/T} \end{cases}$
$H_2CO + OH \rightleftharpoons HOCH_2O$	$k_0 = 7.475 \times 10^{-9} T^{-1.1}$
$HOCH_2O \rightleftharpoons HOCHO + H$	$k_0 = 1.0 \times 10^{14} e^{-7491/T}$
$CH_3OH\ (+M) \rightleftharpoons CH_3 + OH\ (+M)$	$\begin{cases} k_0 = 2.492 \times 10^{19} T^{-6.995} e^{-49270/T} \\ k_\infty = 2.084 \times 10^{18} T^{-0.615} e^{-46530/T} \end{cases}$
$CH_3OH\ (+M) \rightleftharpoons {}^3CH_2 + H_2O\ (+M)$	$\begin{cases} k_0 = 2.375 \times 10^{23} T^{-8.227} e^{-49980/T} \\ k_\infty = 3.121 \times 10^{18} T^{-1.017} e^{-46110/T} \end{cases}$
$CH_3OH\ (+M) \rightleftharpoons CH_2OH + H\ (+M)$	$\begin{cases} k_0 = 5.631 \times 10^{18} T^{-7.244} e^{-52910/T} \\ k_\infty = 7.896 \times 10^{-3} T^{5.038} e^{-42470/T} \end{cases}$
$CH_3OH + H \rightleftharpoons CH_2OH + H_2$	$k_0 = 5.1 \times 10^{-19} T^{2.55} e^{-2735/T}$
$CH_3OH + O_2 \rightleftharpoons CH_3O + OOH$	$k_0 = 5.947 \times 10^{-20} T^{2.27} e^{-21500/T}$
$CH_3OH + OOH \rightleftharpoons CH_3O + H_2O_2$	$k_0 = 2.027 \times 10^{-12} e^{-10090/T}$
$CH_3OH + CH_3OO \rightleftharpoons CH_2OH + CH_3OOH$	$k_0 = 3.007 \times 10^{-12} e^{-6893/T}$
$CH_2OH + OOH \rightleftharpoons HOCH_2O + OH$	$k_0 = 1.661 \times 10^{-11}$
$CH_2OH + O_2 \rightleftharpoons H_2CO + OOH$	$k_0 = 2.508 \times 10^{-9} T^{-1}$
$CH_2OH + O_2 \rightleftharpoons H_2CO + OOH$	$k_0 = 4.003 \times 10^{-10} e^{-2522/T}$
$CH_2OH + HCO \rightleftharpoons CH_3OH + CO$	$k_0 = 1.661 \times 10^{-11}$
$CH_2OH + CH_2OH \rightleftharpoons H_2CO + CH_3OH$	$k_0 = 4.983 \times 10^{-12}$
$CH_3OH + CH_3 \rightleftharpoons CH_2OH + CH_4$	$k_0 = 3.538 \times 10^{-25} T^{3.953} e^{-3547/T}$
$CH_3OH + CH_3 \rightleftharpoons CH_3O + CH_4$	$k_0 = 5.349 \times 10^{-21} T^{2.425} e^{-4313/T}$
$CH_3OH + HCO \rightleftharpoons CH_2OH + H_2CO$	$k_0 = 1.6 \times 10^{-20} T^{2.9} e^{-6591/T}$
$CH_3OH + H \rightleftharpoons CH_3O + H_2$	$k_0 = 3.306 \times 10^{-19} T^{2.56} e^{-5178/T}$
$CH_3OH + O^3P \rightleftharpoons CH_3O + OH$	$k_0 = 6.445 \times 10^{-20} T^{2.5} e^{-1549/T}$
$CH_3OH + O^3P \rightleftharpoons CH_2OH + OH$	$k_0 = 6.445 \times 10^{-19} T^{2.5} e^{-1549/T}$
$CH_3OH + OH \rightleftharpoons CH_3O + H_2O$	$k_0 = 2.492 \times 10^{-22} T^{3.03} e^{383.6/T}$
$CH_3OH + OH \rightleftharpoons CH_2OH + H_2O$	$k_0 = 5.116 \times 10^{-20} T^{2.65} e^{405.6/T}$
$CH_3OH + O_2 \rightleftharpoons CH_2OH + OOH$	$k_0 = 5.947 \times 10^{-19} T^{2.27} e^{-21500/T}$
$CH_3OH + OOH \rightleftharpoons CH_2OH + H_2O_2$	$k_0 = 5.415 \times 10^{-11} e^{-9443/T}$
$CH_3 + OOH \rightleftharpoons CH_3O + OH$	$k_0 = 1.661 \times 10^{-12} T^{0.269} e^{345.7/T}$
$CH_3O\ (+M) \rightleftharpoons H_2CO + H\ (+M)$	$\begin{cases} k_0 = 3.101 \times 10^{1} T^{-3} e^{-12220/T} \\ k_\infty = 6.8 \times 10^{13} e^{-13160/T} \end{cases}$
$CH_3O + O_2 \rightleftharpoons H_2CO + OOH$	$k_0 = 7.276 \times 10^{-43} T^{9.5} e^{2766/T}$
$CH_3O + H \rightleftharpoons H_2CO + H_2$	$k_0 = 3.322 \times 10^{-11}$
$CH_3O + CH_3 \rightleftharpoons H_2CO + CH_4$	$k_0 = 1.993 \times 10^{-11}$
$H_2CO + CH_3O \rightleftharpoons HCO + CH_3OH$	$k_0 = 1.1 \times 10^{-12} e^{-1153/T}$
$C_2H_4 + CH_3O \rightleftharpoons C_2H_3 + CH_3OH$	$k_0 = 1.993 \times 10^{-13} e^{-3394/T}$
$2\,OH\ (+M) \rightleftharpoons H_2O_2\ (+M)$	$\begin{cases} k_0 = 1.526 \times 10^{-28} T^{-0.76} \\ k_\infty = 1.201 \times 10^{-10} T^{-0.37} \end{cases}$
$CO + OH \rightleftharpoons CO_2 + H$	$k_0 = 4.983 \times 10^{-20} T^{1.5} e^{251.4/T}$

Notes. These reactions are either totally new compared to the former scheme, or the reaction rate has been modified. The corresponding reaction rates are expressed with a modified Arrhenius law $k(T) = A \times T^n \exp^{-\frac{E_a}{RT}}$, with T in Kelvin, E_a/R in Kelvin, and n dimensionless. k_0 and k_∞ are the reaction rates in the low and high pressure regimes, respectively. For k_0, unit of A is as follows: $s^{-1}\,K^{-n}$ for thermal dissociations, cm^3 molecule^{-1} s^{-1} K^{-n} for bimolecular reactions or decomposition reaction with a second-body M, and cm^6 molecule^{-2} s^{-1} K^{-n} for combination reactions with a third-body M. For k_∞, unit of A is as follows: $s^{-1}\,K^{-n}$ for decomposition reactions (behavior of a thermal dissociation), and cm^3 molecule^{-1} s^{-1} and K^{-n} for combination reactions (behavior of bimolecular reactions).

Table B.2. Reactions of the new chemical sub-network of CH_3OH involving a logarithmic dependence with pressure, extracted from Burke et al. (2016).

Reaction	Rate
$CH_3 + OH \rightleftharpoons HCOH + H_2$	$k_0 = \begin{cases} 1.441 \times 10^{-15} T^{0.787} e^{1531/T}, p = 0.01\,\text{atm} \\ 5.173 \times 10^{-15} T^{0.630} e^{1343/T}, p = 0.1\,\text{atm} \\ 2.585 \times 10^{-13} T^{0.156} e^{688/T}, p = 1\,\text{atm} \\ 2.830 \times 10^{-3} T^{-2.641} e^{3227/T}, p = 10\,\text{atm} \\ 1.204 \times 10^{-3} T^{-2.402} e^{4851/T}, p = 100\,\text{atm} \end{cases}$
$CH_3 + OH \rightleftharpoons CH_2OH + H$	$k_0 = \begin{cases} 2.692 \times 10^{-14} T^{0.965} e^{-1617/T}, p = 0.01\,\text{atm} \\ 3.001 \times 10^{-14} T^{0.950} e^{-1632/T}, p = 0.1\,\text{atm} \\ 7.781 \times 10^{-14} T^{0.833} e^{-1794/T}, p = 1\,\text{atm} \\ 2.532 \times 10^{-11} T^{0.134} e^{-2839/T}, p = 10\,\text{atm} \\ 5.961 \times 10^{-10} T^{-0.186} e^{-4328/T}, p = 100\,\text{atm} \end{cases}$
$CH_3 + OH \rightleftharpoons H + CH_3O$	$k_0 = \begin{cases} 1.969 \times 10^{-15} T^{1.016} e^{-6008/T}, p = 0.01\,\text{atm} \\ 1.973 \times 10^{-15} T^{1.016} e^{-6008/T}, p = 0.1\,\text{atm} \\ 2.042 \times 10^{-15} T^{1.011} e^{-6013/T}, p = 1\,\text{atm} \\ 2.986 \times 10^{-15} T^{0.965} e^{-6069/T}, p = 10\,\text{atm} \\ 8.705 \times 10^{-14} T^{0.551} e^{-6577/T}, p = 100\,\text{atm} \end{cases}$
$C_2H_3 + O_2 \rightleftharpoons CO + CH_3O$	$k_0 = \begin{cases} 1.360 \times 10^{-5} T^{-2.66} e^{-1611/T}, p = 0.01\,\text{atm} \\ 6.742 \times 10^{-10} T^{-1.32} e^{-446/T}, p = 0.1\,\text{atm} \\ 7.207 \times 10^{-10} T^{-1.33} e^{-453/T}, p = 0.316\,\text{atm} \\ 1.710 \times 10^{-13} T^{-0.33} e^{376/T}, p = 1\,\text{atm} \\ 3.138 \times 10^{-12} T^{-3.00} e^{4526/T}, p = 3.16\,\text{atm} \\ 3.205 T^{-5.63} e^{-1/T}, p = 10\,\text{atm} \\ 1.827 \times 10^{-6} T^{-2.22} e^{-2606/T}, p = 31.6\,\text{atm} \\ 9.615 \times 10^{8} T^{-6.45} e^{-8459/T}, p = 100\,\text{atm} \end{cases}$
$C_2H_3 + O_2 \rightleftharpoons CO + CH_3O$	$k_0 = \begin{cases} 2.142 \times 10^{-15} T^{0.18} e^{864/T}, p = 0.01\,\text{atm} \\ 9.947 \times 10^{-13} T^{-2.93} e^{4813/T}, p = 0.1\,\text{atm} \\ 4.832 \times 10^{-13} T^{-2.93} e^{5093/T}, p = 0.316\,\text{atm} \\ 9.581 \times 10^{-3} T^{-3.54} e^{-2401/T}, p = 1\,\text{atm} \\ 8.286 \times 10^{-9} T^{-1.62} e^{-930/T}, p = 3.16\,\text{atm} \\ 1.549 \times 10^{-7} T^{-1.96} e^{-1673/T}, p = 10\,\text{atm} \\ 1.694 \times 10^{48} T^{-20.69} e^{-7981/T}, p = 31.6\,\text{atm} \\ 1.827 \times 10^{-15} T^{0.31} e^{-515/T}, p = 100\,\text{atm} \end{cases}$
$C_2H_5OH \rightleftharpoons CH_3 + CH_2OH$	$k_0 = \begin{cases} 1.20 \times 10^{54} T^{-1.29} e^{-50330/T}, p = 0.001\,\text{atm} \\ 5.18 \times 10^{59} T^{-14.0} e^{-50280/T}, p = 0.01\,\text{atm} \\ 1.62 \times 10^{66} T^{-15.3} e^{-53040/T}, p = 0.1\,\text{atm} \\ 5.55 \times 10^{64} T^{-14.5} e^{-53430/T}, p = 1\,\text{atm} \\ 1.55 \times 10^{58} T^{-12.3} e^{-53230/T}, p = 10\,\text{atm} \\ 1.78 \times 10^{47} T^{-8.96} e^{-50860/T}, p = 100\,\text{atm} \end{cases}$

Notes. The corresponding reaction rates are expressed with a modified Arrhenius law $k_0(T) = A \times T^n \exp^{-\frac{E_a}{RT}}$, with T in Kelvin, E_a/R in Kelvin, and n dimensionless. The value A is in $s^{-1}\,K^{-n}$ for the thermal dissociation and $cm^3\,molecule^{-1}\,s^{-1}\,K^{-n}$ for bimolecular reactions.

reactions of the new CH_3OH sub-scheme that present an explicit logarithmic dependence with pressure. The chemical rate of such a reaction is computed by interpolating over pressure at the considered temperature.

Appendix C: Validation of the new chemical scheme

In what follows, we present model comparisons with experimental data for the cases in which the new CH_3OH sub-scheme improvement is most noticeable. Burke et al. (2016) studied the combustion of methanol in a shock tube at several pressures and temperatures. Figure C.1 shows, for the chemical scheme of Venot et al. (2012) and the new scheme of this paper, the variations of the autoignition are delayed times at two different pressures (10 and 50 bar), for temperatures ranging from 1000 to 1500 K and for an equivalence ratio of 1. We also include simulations with the new scheme compared with the data from Fieweger et al. (1997) at 13 bar.

The study of the pyrolysis of methanol at a very high temperature of about 2000 K and low pressure, around 0.4 atm, in a shock tube by Cribb et al. (1984) is shown in Fig. C.2. The variation of mole fraction of different compounds obtained in a batch reactor obtained by Cathonnet et al. (1982) at relatively low temperature, around 800 K, is presented in Fig. C.2.

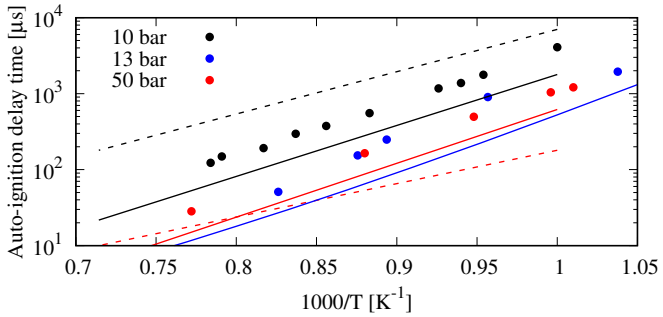

Fig. C.1. Autoignition delay times of methanol in shock tube under high pressure. The points represent experimental data from Burke et al. (2016) and Fieweger et al. (1997), and the lines show simulations with the chemical scheme of Venot et al. (2012) (dashed) and with the updated chemical scheme of this paper (solid). Composition: 5.7 mol% CH_3OH+8.55 mol% O_2 + N_2.

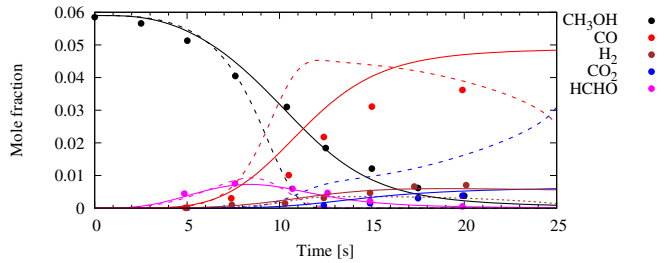

Fig. C.2. Species profiles for static reactor experiments where symbols denote experimental measurements from Cathonnet et al. (1982) and curves modeling results using the chemical scheme of Venot et al. (2012) (dashed) and with the updated chemical scheme of this paper (solid). Experimental conditions: 5.89 mol% CH_3 + 8.84 mol% O_2 + N_2, T = 823 K, P = 0.026 MPa.

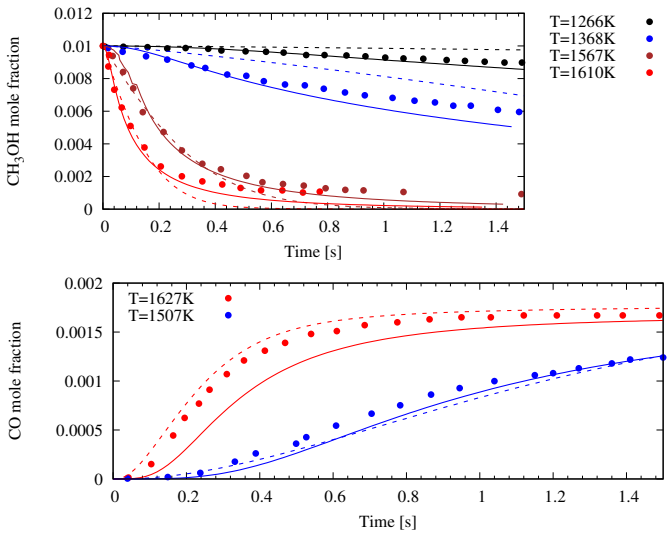

Fig. C.3. Mole fraction of methanol (*top*) and carbon monoxide (*bottom*) versus time for the combustion of methanol in a shock tube for a pressure around 2.5 atm, and an equivalence ratio of 1. The points represent experimental data from Ren et al. (2013), and the lines show modeling results using the chemical scheme of Venot et al. (2012) (dashed) and with the updated chemical scheme of this paper (solid). P = 2.2 atm, (right) P = 1.1 atm.

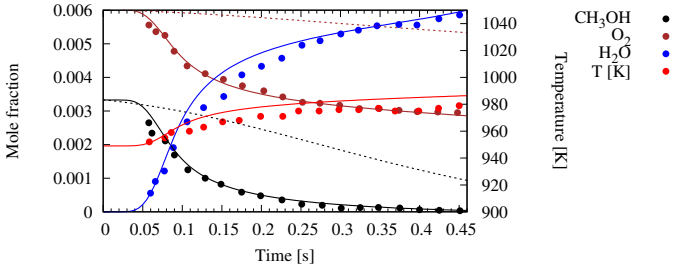

Fig. C.4. Reaction profiles of CH_3OH/air mixtures in a flow reactor, where symbols represent the experimental data of Held & Dryer (1994) and curves modeling results using the chemical scheme of Venot et al. (2012) (dashed lines) and with the updated chemical scheme of this paper (solid lines). Experimental conditions: 0.33 mol% CH_3OH + 0.6 mol% O_2 + N_2, T around 1000 K, P = 0.25 MPa.

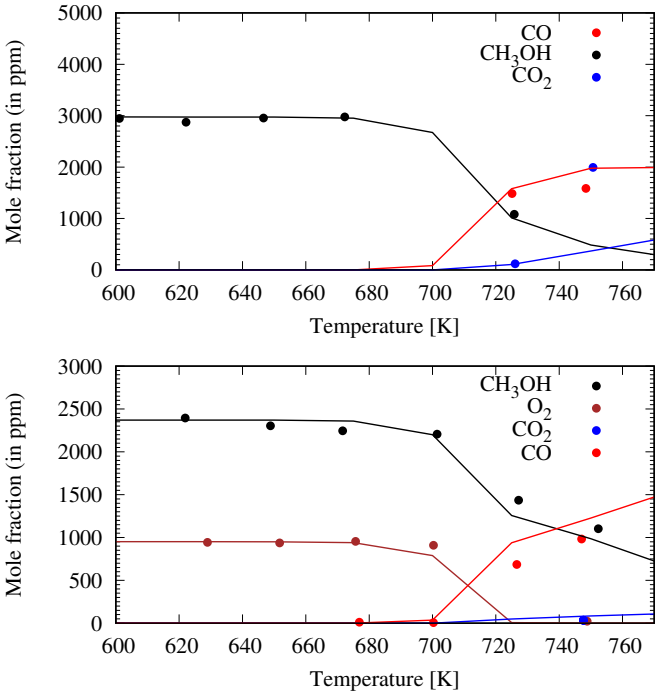

Fig. C.5. High pressure (100 bar) CH_3OH combustion experimental data (dots) of Aranda et al. (2013) in lean (*top*) and fuel-rich (*bottom*) conditions compared to our new chemical model simulations (solid lines).

Figure C.3 shows the variation of mole fraction of methanol and carbon monoxide versus time obtained in a shock tube during the pyrolysis of methanol diluted in Argon (1/99) at various temperatures and for a pressure of 2.2 and 1.1 atm by Ren et al. (2013).

In addition, we compared the experimental data of Held & Dryer (1994) obtained in a plug flow reactor against simulated results with the updated chemical scheme of this paper, at a pressure of 0.26 MPa and a temperature around 1000 K (see Fig. C.4).

We also checked the high pressure regime to test the PLOG formalism for some kinetic rates (see Table B.2), and we find a good agreement for our new chemical scheme with the data from Aranda et al. (2013), as shown in Fig. C.5.

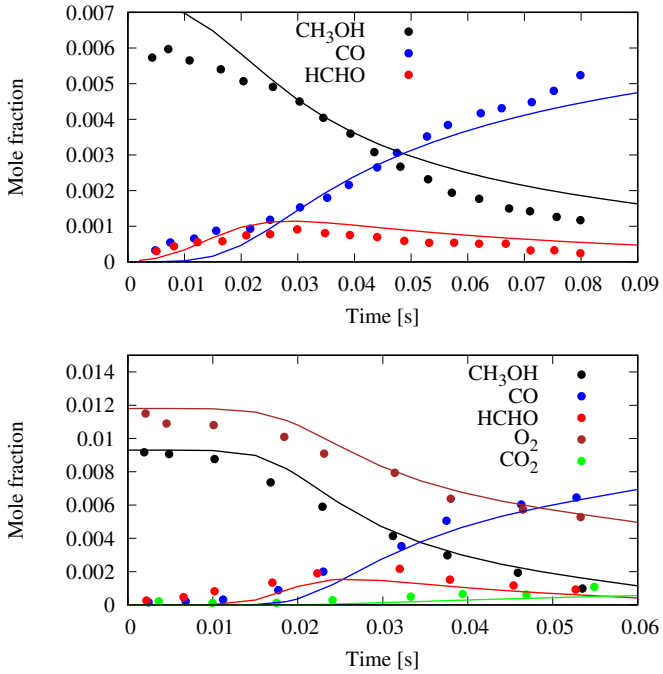

Fig. C.6. Species mole fractions vs. time in a plug flow reactor. Solid lines are obtained from simulations using updated chemical scheme of this paper. *Top*: $p = 1$ atm, $T = 1000$ K, 6200 ppm CH_3OH + 6500 ppm O_2 balanced with N_2, (Aronowitz et al. 1979). *Bottom*: $P = 1$ atm, $T = 1031$ K, 9300 ppm CH_3OH + 11800 ppm O_2 balanced with N_2 (Norton & Dryer 1989).

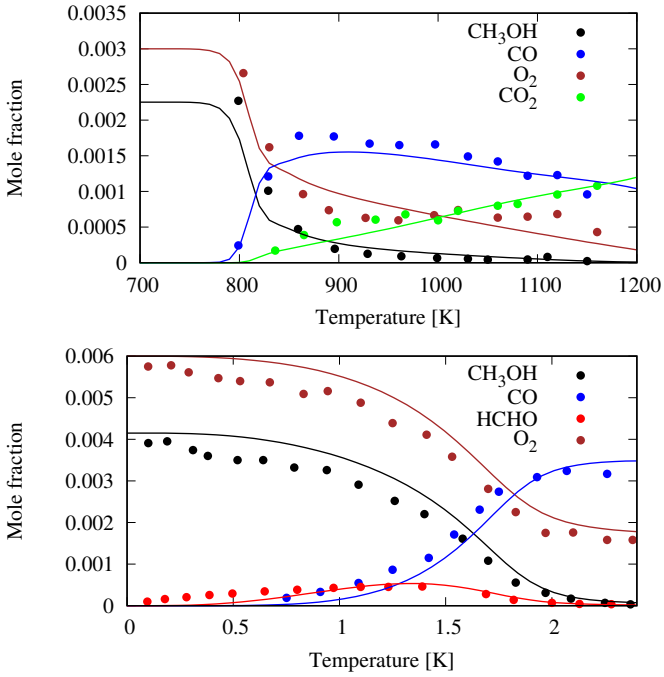

Fig. C.7. Species mole fractions vs. temperature and time. *Top panel*: experiment conducted with a jet-stirred reactor. Experimental conditions: $P = 20$ atm, equivalence ratio = 1, 2400 ppm CH_3OH + 3000 ppm O_2 balanced with N_2 (Burke et al. 2016). *Bottom panel*: experiment conducted with a plug flow reactor. Experimental conditions are $P = 1$ atm, 4150 ppm CH_3OH + 6000 ppm of O_2 balanced with N_2, $T = 783$K, $P = 15$ atm (Held & Dryer 1994). Data are compared with simulations using the updated chemical scheme of this paper (solid lines).

Finally, comparisons in Figs. C.6 and C.7 demonstrate that the predictions from the new sub-mechanism of methanol oxidation are in good agreement with the species time and temperature history measurements in plug flow or jet-stirred reactors at various pressures (Aronowitz et al. 1979; Norton & Dryer 1989; Held & Dryer 1994; Burke et al. 2016).

Appendix D: New reduced chemical scheme

A reduced chemical scheme of V12 was recently developed by Venot et al. (2019) to reproduce the abundances of H_2O, CH_4, CO, CO_2, NH_3, and HCN, i.e., species already detected in (exo)planet atmospheres. Following our update of the former full scheme, we also provide an update for the reduced scheme. We derived the new reduced scheme by following the same methodology as in Venot et al. (2019). We used the ANSYS Chemkin-Pro® Reaction Workbench package via the method Directed Relation Graph with Error Propagation (DRGEP), followed by a Sensitivity Analysis. After several reduction attempts, we ended with the reduced scheme presented in this work. It is the best compromise between number of species, number of reactions, applicability range, and abundances accuracy. As in Venot et al. (2019), the scheme has been developed primarily for GJ 436b-like planets to reproduce the abundances of the current observed neutral species (listed previously), as well as C_2H_2, but it can be applied to hot Jupiters, brown dwarfs, and Solar System giant planets as well. Acetylene was not included in the former reduced scheme, which prevented its use for modeling very hot C-rich atmospheres. Thus, this updated reduced network is sensibly larger than the previous network (i.e., 30 species, 181 reversible reactions) and contains 44 species, 288 reversible and 6 irreversible reactions, i.e., a total of 582 reactions. Like the updated full chemical scheme, it is available on KIDA (Wakelam et al. 2012).

The updated reduced scheme gives very good results for the planets modeled in this study (see Figs. D.1–D.3). In order to show the validity of the reduced scheme for hot C-rich atmospheres, we modeled HD 209458b with a high C/O ratio (3⊙), following Venot et al. (2019). While CH_4 was clearly overestimated in the upper atmosphere with the reduced scheme of Venot et al. (2019, see their Fig. 11), our new reduced scheme provides a better agreement for CH_4 thanks to the addition of C_2H_2 in the scheme.

For each species of interest, the maximum difference of abundances obtained using the two chemical networks (with the corresponding pressure level) are gathered in Tables D.1–D.3. For the exoplanets and the brown dwarf, we restricted our comparison to the pressure range probed by observations. For the Solar System giant planets, we focused on the quenching area, as this level governs the abundances observed at 2 bar and is thus decisive for the conclusions drawn regarding their elemental composition (Cavalié et al. 2009, 2014, 2017). For GJ 436b, ULAS J1335+11, Uranus, and Neptune, variations are below 10%. We notice that a lower agreement is found for hot Jupiter atmospheres, especially in the upper atmosphere of HD 209458b, where the pressure is low and the temperature high. However, we checked via the `TauRex` code in forward mode that these variations occur high enough in the atmosphere and do not impact the synthetic spectra computed with these two chemical compositions. We note that the comparison is made for models without photodissociation because the reduced scheme does not contain photolysis reactions.

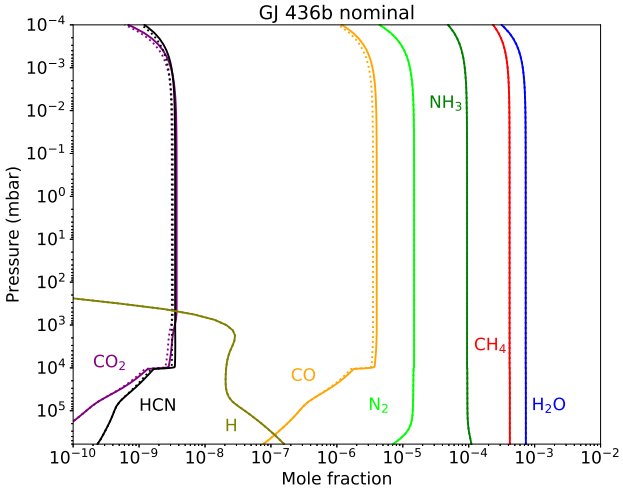

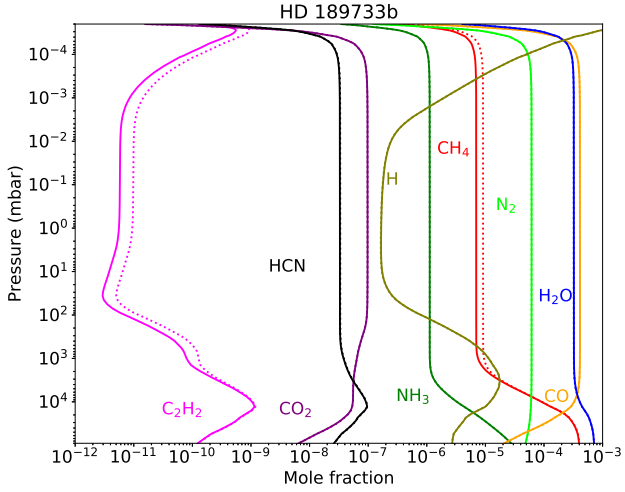

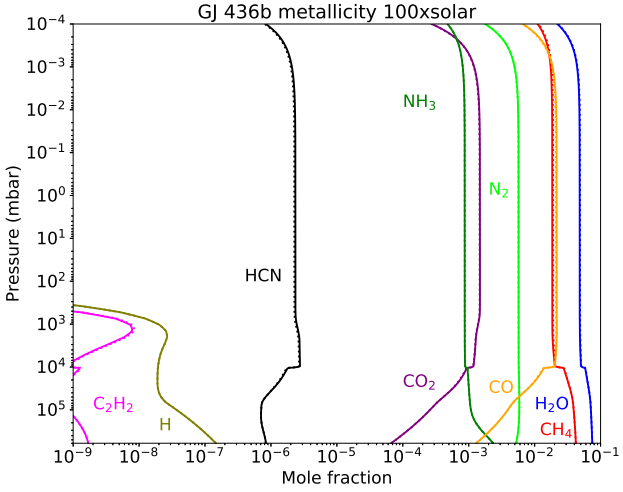

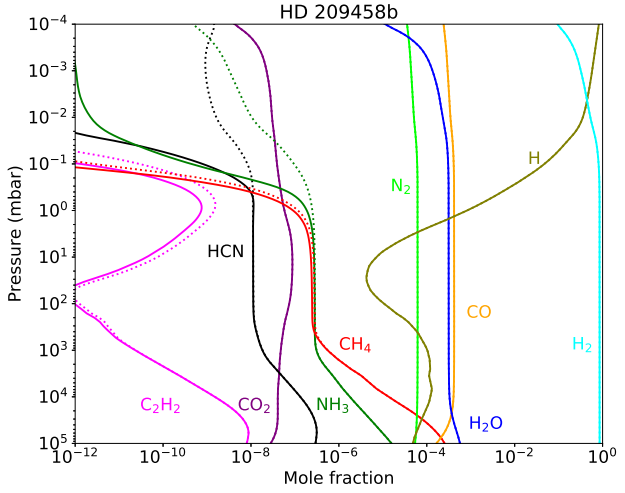

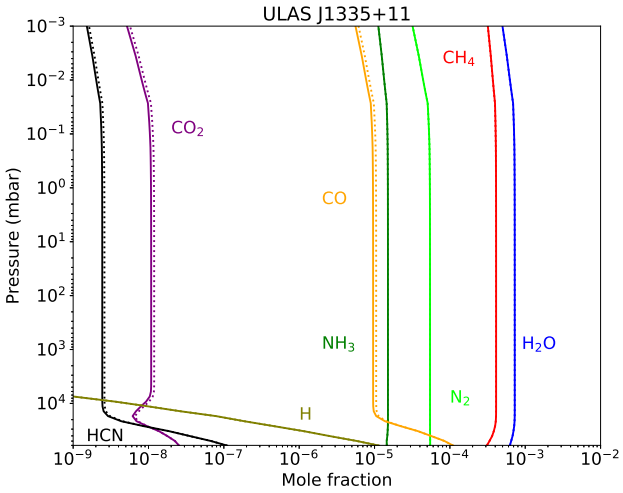

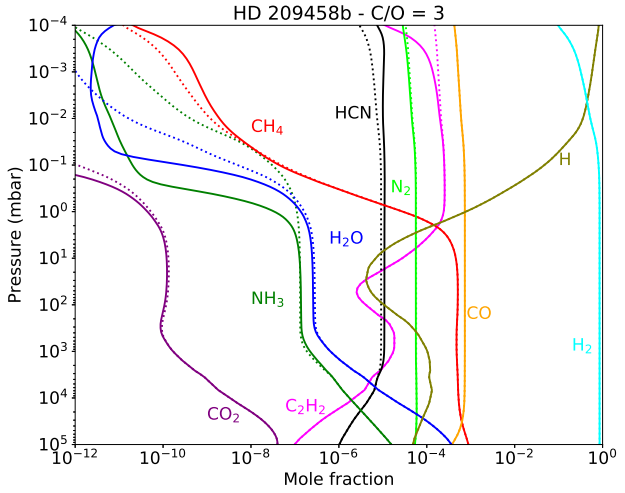

Fig. D.1. Vertical abundances profiles of the main species in GJ 436b with a solar metallicity (*top*), with a metallicity of 100⊙ (*middle*), and in ULAS J1335+11 (*bottom*). The abundances obtained with the updated chemical scheme (solid lines) are compared to those obtained with the reduced scheme (dotted lines).

Fig. D.2. Vertical abundances profiles of the main species in HD 189733b (*top*), HD 209458b (*middle*), and HD 209458b with a C/O ratio of 3⊙ (*bottom*). The abundances obtained with the updated chemical scheme (solid lines) are compared to those obtained with the reduced scheme (dotted lines).

Table D.1. For GJ 436b models, with different metallicities, and the ULAS J1335+11 model, maximum variations of abundances (in %) for each species for which the reduced scheme is designed.

Species	GJ 436b	GJ 436b, $Z = 100\odot$	ULAS J1335+11
H_2O	7×10^{-2} (@6×10^{2})	1 (@6×10^{-1})	1×10^{-1} (@6×10^{3})
CH_4	2×10^{-1} (@6×10^{2})	3 (@3×10^{2})	2×10^{-1} (@1×10^{1})
CO	1×10^{1} (@1×10^{-1})	2 (@1×10^{-1})	1×10^{1} (@6×10^{3})
CO_2	1×10^{1} (@1×10^{-1})	1 (@1×10^{-1})	1×10^{1} (@5×10^{3})
NH_3	2×10^{-2} (@8×10^{2})	2×10^{-1} (@9×10^{2})	3×10^{-3} (@5×10^{4})
HCN	1×10^{1} (@1×10^{-1})	3 (@1×10^{-1})	7 (@7×10^{3})
C_2H_2	4×10^{-1} (@6×10^{-1})	8 (@1)	5×10^{-1} (@1×10^{3})

Notes. The pressure level (@level in mbar) at which the maximum variation is reached is indicated within parentheses. These values are calculated within the regions probed by infrared observations: i.e., [0.1–1000] mbar and [10–10^4] mbar for the warm Neptune and the T Dwarf, respectively.

Table D.2. For HD 209458b models, with different C/O ratios, and HD 189733b models, with different eddy diffusion coefficients, maximum variations of abundances (in %) for each species for which the reduced scheme is designed.

Species	HD 209458b	HD 209458b, C/O = $3\odot$	HD 189733b
H_2O	1×10^{-1} (@9×10^{2})	1×10^{3} (@1×10^{-1})	5×10^{-1} (@1×10^{3})
CH_4	1×10^{3} (@1×10^{-1})	1×10^{1} (@1×10^{-1})	3×10^{1} (@3×10^{1})
CO	9×10^{-2} (@9×10^{2})	8×10^{-3} (@6×10^{-1})	4×10^{-1} (@1×10^{3})
CO_2	4×10^{-2} (@9×10^{2})	1×10^{3} (@1×10^{-1})	8×10^{-2} (@1×10^{-1})
NH_3	2×10^{4} (@1×10^{-1})	2×10^{5} (@1×10^{-1})	4×10^{-1} (@1×10^{-1})
HCN	8×10^{2} (@1×10^{-1})	2×10^{1} (@1×10^{-1})	1 (@1×10^{3})
C_2H_2	2×10^{3} (@1×10^{-1})	9×10^{-1} (@7×10^{1})	7×10^{1} (@2×10^{2})

Notes. The pressure level (@level in mbar) at which the maximum variation is reached is indicated in parentheses. These values are calculated within the region probed by infrared observations ([0.1–1000] mbar).

Table D.3. For Uranus and Neptune models, maximum differences of abundances (in %) for each species for which the reduced scheme is designed.

Species	Uranus	Neptune
H_2O	9×10^{-4} (@8×10^{6})	2×10^{-4} (@2×10^{6})
CH_4	2×10^{-2} (@8×10^{6})	4×10^{-3} (@8×10^{6})
CO	1×10^{1} (@8×10^{6})	8 (@1×10^{6})
CO_2	8 (@1×10^{6})	6 (@1×10^{6})
NH_3	8×10^{-4} (@8×10^{6})	2×10^{-4} (@8×10^{6})
HCN	4×10^{-1} (@3×10^{6})	3 (@2×10^{6})
C_2H_2	4×10^{-2} (@8×10^{6})	1×10^{-2} (@1×10^{6})

Notes. The pressure level (@level in mbar) at which the maximum variation is reached is indicated in parentheses. These values are calculated within the region where quenching occurs ([10^6–10^7] mbar).

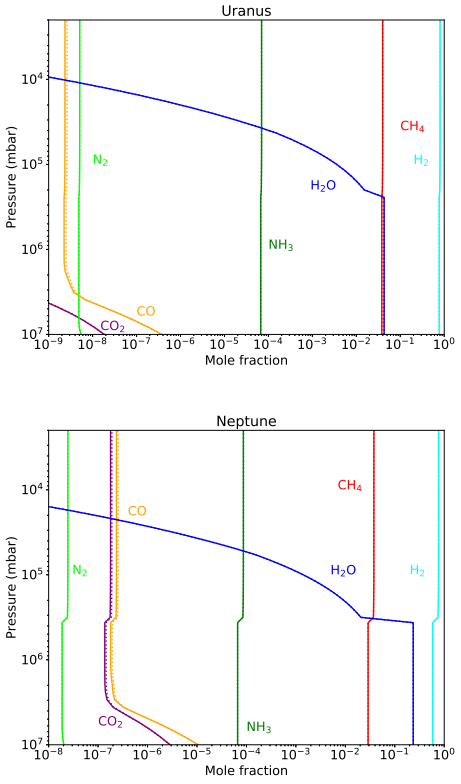

Fig. D.3. Vertical abundances profiles of the main species in Uranus (*top*) and Neptune (*bottom*). The abundances obtained with the updated chemical scheme (solid lines) are compared to those obtained with the reduced scheme (dotted lines).